EDMOND C. ROELOF and DONALD J. WILLIAMS

THE TERRESTRIAL RING CURRENT: FROM *IN SITU* MEASUREMENTS TO GLOBAL IMAGES USING ENERGETIC NEUTRAL ATOMS

Electrical currents flowing in the equatorial magnetosphere, first inferred from ground-based magnetic disturbances, are carried by trapped energetic ions. Spacecraft measurements have determined the spectrum and composition of those currents, and the newly developed technique of energetic-neutral-atom imaging allows the global dynamics of that entire ion population to be viewed from a single spacecraft.

INTRODUCTION

Conceptually, the motion of a single charged particle constitutes an electric current. In reality, it is the collective motion of many such particles that constitutes the more familiar macroscopic current systems encountered in nature. In the presence of a magnetic field, the individual particle trajectories are curved, and the resulting current density becomes geometrically complex, so that, except for a few important but restrictive cases, it is difficult to visualize. For a hot ionized gas (a plasma), the concept of individual trajectories must be replaced by an even more complex collective description of the plasma as a whole. The generation and the behavior of electric currents in a magnetic field are problems of fundamental interest that bear directly on our understanding of numerous magnetized plasma environments found throughout the cosmos in planetary magnetospheres, the heliosphere, solar systems (during their formation), neutron stars, and entire galaxies.

Current flow induces a secondary magnetic field (as described by Ampere's law) and distorts the ambient magnetic field over a wide range of spatial and temporal scales. To some extent the distortions may be used to infer the geometry of the current flow.[1] In the case of the earth, they also adversely affect numerous operational systems, such as communications and electric power systems, both in space and at the earth's surface.[2] Such effects underscore the importance of the high-altitude (space) boundary condition in earth environmental studies and add a pragmatic incentive to solve this scientific problem.

The earth's geomagnetic field, considered along with the particles contained therein (i.e., the magnetosphere), is a good example of a dynamic astrophysical system that illustrates the development of currents from charged particle distributions in magnetic fields. Figure 1 is a simplified schematic of the earth's magnetosphere. The magnetosphere is confined by the flowing solar-wind plasma to an altitude of approximately 10 R_e (R_e = 6370 km, a mean value for the earth's radius) near local noon. On the nightside, the earth's magnetic field lines extend outward in the antisolar direction to form a magnetotail that is measurable to distances of several million kilometers.

Numerous charged particle populations reside within the magnetospheric cavity (Fig. 1a); they include a hot plasma sheet in the magnetotail consisting of ion and electron populations with temperatures of about 10 keV (1 keV $\approx 1.2 \times 10^7$ K), as well as the familiar trapped particle populations. Among this latter group resides the ring current, a population of trapped ions encircling the earth; it is responsible for the observed worldwide decreases in the earth's surface magnetic field that are known as magnetic storms. Extending earthward from the ring current and merging with the ionosphere is the plasmasphere, a cold plasma ($\lesssim$0.3 eV) that plays an active role in ring-current behavior.

The recent energetic-ion measurements from the Active Magnetospheric Particle Tracer Explorers/Charge Composition Explorer (AMPTE/CCE) spacecraft[3,4] have established that the ring current consists of energetic ($\sim$1–200 keV) ions that are trapped in the earth's magnetic field on field lines crossing the equator at distances between about 2.5 and 8 R_e. Protons and singly charged oxygen ions (O^+) are the main constituents of the ring current, and protons of energy 20 to 200 keV make up the bulk of the current system.

Figures 1b and 1c also show the time evolution and global structure of the observed ground-level magnetic signatures of the storm-time ring-current system. The average hourly value of the magnetic disturbance at

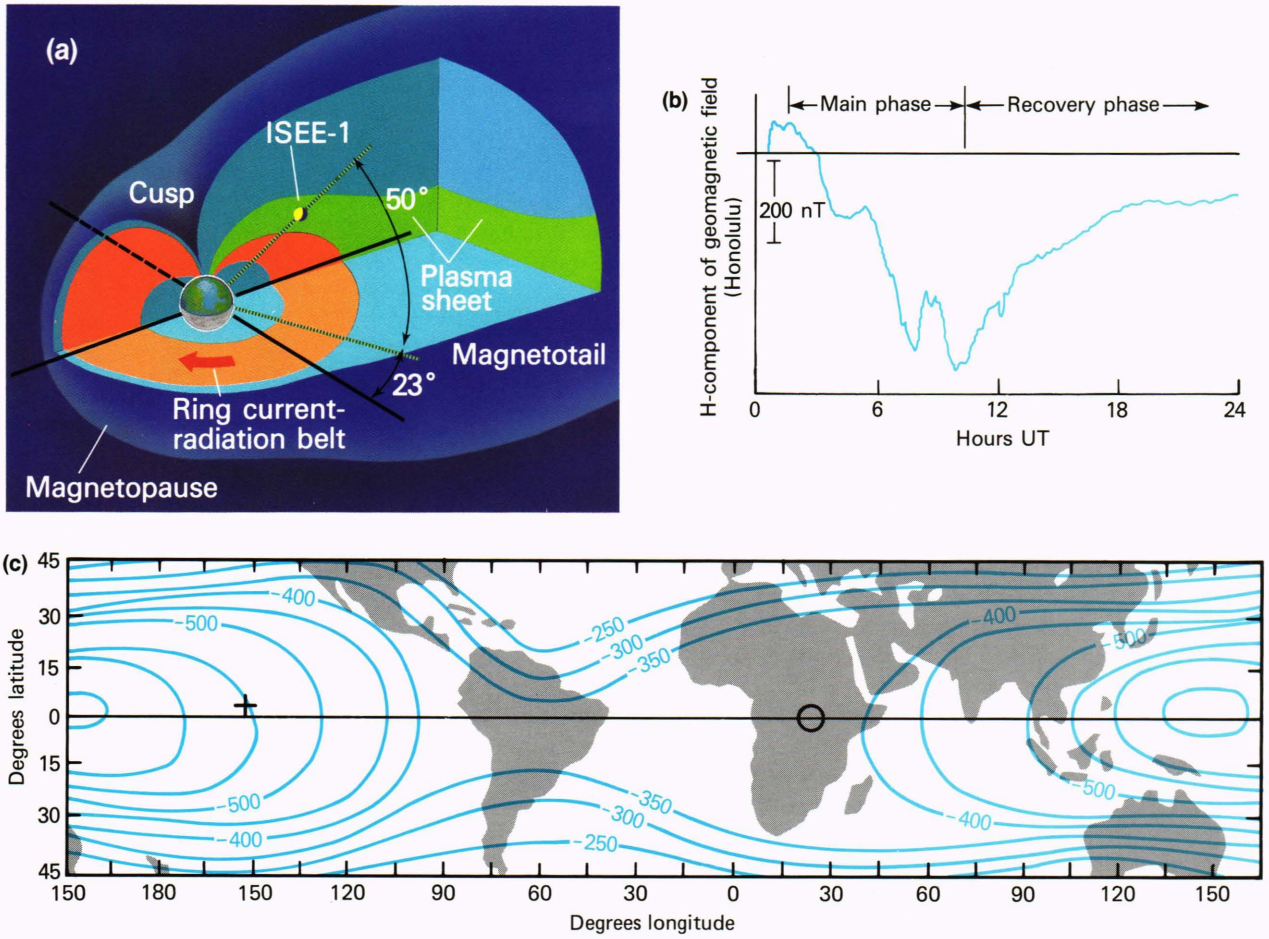

Figure 1 — (a) Populations of energetic ions (approximately 100 keV) in the magnetosphere. The major constituents of the ring current are 20- to 200-keV singly charged hydrogen and oxygen ions. (b) Time evolution of the low-latitude surface perturbation of earth's magnetic field for the magnetic storm of 13 September 1957. Ring-current intensification occurs during the main phase and decay in the recovery phase. (c) Iso-intensity contours (nT) of worldwide magnetic perturbations during the great magnetic storm of 13 September 1957. Strong anisotropy, implying intense ring current west of local midnight at 1100 and 1200 UT (+ sign on figure), relaxes hours later in the recovery phase of storm.

equatorial stations (Fig. 1b) is called D_{st} (for disturbance, storm) and can exceed 200 nT in large storms (1 nT = 10^{-5}G). As mentioned above, the actual currents produced by the ring-current ions are not easily visualized and must be calculated from observed ion fluxes. Within any given hour of a storm, contours of the reduction of the meridional (H) component of the surface magnetic field can be constructed at ground observatories, as shown in Fig. 1c.

Note that observations of the magnetic perturbations made only at the earth's surface do not allow unique, accurate inferences about global ring-current characteristics. That is because the ring current lies outside the surface on which those measurements are made.

The ring current provides an excellent case study of the problem of the generation and behavior of electric currents in a magnetized plasma. That problem has been apparently "solved" several times in the past—solved in the sense that the source, geometry, energy, and composition of the ring current were considered to be understood at the time. As new data became available, however, the previous solutions were found lacking, and researchers approached the problem anew, armed with the results of past efforts. This process continues today. *In situ* satellite observations have located the ring-current ion population within the earth's magnetic field, established the particle energies and intensities involved, measured the ion angular distributions on a given magnetic field line, and, most recently, determined the composition of the ions responsible for the ring current.

However, because the *in situ* measurements are local observations along a satellite orbit, little is known about the instantaneous global structure of ring-current ion fluxes and their evolution. As we have mentioned, an understanding of the dynamics and the calculation of the actual currents produced by the ring-current ions require a global description of their flux distribution. Since we have not known the global structure of the ring-current ion fluxes, we have been unable to describe the global ring-current system accurately.

The recently proven technique of energetic-neutral-atom (ENA) imaging, however, permits observation of

the global structure and evolution of the ring-current ion population. Global images of the ion population will allow the first accurate determination of the global current system that constitutes the ring current. Before describing the new technique, we will first describe our present understanding of the ring current and its dynamics.

PARTICLE DISTRIBUTIONS AND CURRENTS

The idea that electric currents flowing in space might be responsible for auroral phenomena and magnetic field variations observed at the earth's surface dates back to the 19th century and the pioneering research of Karl Friedrich Gauss.[5] The work of Kristian Birkeland and Carl Störmer in Norway led to the concept that charged particles emitted from the sun had access via the earth's magnetic field to the high-latitude (auroral) regions above the earth's atmosphere and could be responsible for the observed magnetic variations. However, Störmer's calculations showed that charged particles incident on the earth's dipole field from great distances could not gain access to certain "forbidden" regions: closed volumes that were near the earth and encompassed the magnetic equatorial regions. In spite of that result, which seemingly ruled out an equatorial current system close to the earth, Störmer postulated the existence of a distant partial ring of current in the equatorial plane (but outside the forbidden region) to explain the movement of the aurora equatorward during strong magnetic storms. Adolph Schmidt[6] extended the concept of the equatorial current, calling it the "Birkeland–Störmersche ring," and attempted an explanation of the evolution of magnetic storms reported worldwide by observatories in near-equatorial regions. Many of these ideas came to fruition in the early 1930s when Chapman and Ferraro performed detailed calculations of the effects and the stability of an electrically neutral stream of ionized particles from the sun impinging on the earth's magnetic field.[7] Although they were unable to account satisfactorily in the model for the formation of the ring current itself, they were able to account for the storm's sudden commencement. They then simply assumed the existence of a ring current once the storm had begun, and investigated its properties.

Since those early pioneering studies, many theories and experiments have made it possible to identify the particle population making up the ring current and to establish its general location in the magnetosphere.[8-19] In the following we summarize our theoretical and observational understanding of the earth's ring-current system.

THEORETICAL CONCEPTS

We begin by deriving a simple relationship between the total energy of the ions making up the ring current and the reduction in the magnetic field that they produce at the earth's surface.

The orbit of a trapped ion in a dipole-like magnetic field $\bar{B}$ is a complex spiral about the field line plus an average drift motion across the field. In a steady-state (or sufficiently slowly varying) magnetic field, there is a cross-field ($\bar{E} \times \bar{B}$) drift caused by an electric field ($\bar{E}$), in addition to drifts caused by inhomogeneities in the magnetic field (gradient and curvature drifts). Since the $\bar{E} \times \bar{B}$ drift affects all charged particles in the same way (regardless of mass and total charge), it does not, in itself, generate an electric current in a collisionless plasma. The inhomogeneity drifts, on the other hand, are proportional to energy E per charge (E/q) and depend on the particle's pitch angle α (where α is the instantaneous angle between the particle's velocity vector and the local magnetic field vector). The drift velocity is then

$$\bar{v}_D = (E/qB)\,\hat{B} \times (\sin^2\alpha \nabla B + 2\cos^2\alpha \bar{B} \cdot \nabla \hat{B}) \,. \quad (1)$$

The sense of this motion is shown in Fig. 2. The first term of Eq. 1 gives the gradient drift, and the second gives the curvature drift ($\hat{B} \cdot \nabla \hat{B}$ is the curvature vector for a magnetic field line whose direction is given by the unit vector $\hat{B} = \bar{B}/B$).

For our first example of ring-current effects, we take the simplest orbit, one where the particle mirrors near the magnetic equator ($\alpha = 90°$). The center of its gyration drifts westward (i.e., opposite the sense of the earth's rotation) at constant radius around the earth with velocity

$$v_D = -3Er^2/qM \,, \quad (2)$$

where M is the earth's dipole moment, so that, in the equatorial plane, $B = \mu_0 M/4\pi r^3$. By Ampere's law, the magnetic field perturbation produced at the center of the earth by the drift current $qv_D/2\pi r$ of this single particle is

$$\delta B_1 = \mu_0 i/2\pi r = -3\mu_0 E/4\pi M \,. \quad (3)$$

The field produced at the surface of the earth is not much different from the field at the earth's center if the particle gyrocenter lies several earth radii out. The minus sign indicates that δB_1 reduces the dipole field at the surface. This is not the only reduction, because the gyration motion also produces a current that has a mag-

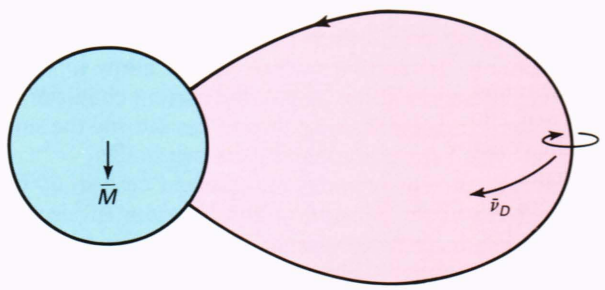

Figure 2 — The earth's dipole field. Field line direction and proton gyration and drift are indicated. See the section on theoretical concepts for discussion.

netic dipole field with moment $\mu = E/B$. The contribution that this small dipole makes at the earth's center is

$$\delta B = (\mu_0/4\pi)(\mu/r^3) = \mu_0 E/4\pi M \ . \qquad (4)$$

Thus, the total field perturbation at the origin caused by the drift and gyration of a single particle at the equator is

$$\delta B = \delta B_1 + \delta B_2 = -\mu_0 E/2\pi M \ . \qquad (5)$$

If we express δB as the fractional change in the surface field B_s, we find a very simple relationship for the magnetic perturbation at the center of the earth caused by a single trapped particle at the magnetic equator:

$$\delta B/B_s = -2E/3U \ , \qquad (6)$$

where U is the total energy in the dipole field exterior to earth's surface, and $U = 4\pi M B_s/3\mu_0$. This result, known as the Dessler–Parker[11] relation, has been shown to hold for any distribution of stably trapped particles in the earth's magnetic field;[20-23] E then becomes the total energy of all the ring-current particles. When the particle kinetic energy density is comparable to or greater than the local magnetic field energy density, the accuracy of this relation deteriorates by about a factor of 2 (because the dipole field is distorted by the ring current itself). For reference, it requires 4×10^{13} J of particle kinetic energy to produce a surface magnetic field depression of 1 nT. In a large geomagnetic storm (Figs. 1b and 1c), the depression can exceed 250 nT (about 1% of the equatorial surface field), so the energy in the storm-time ring current can exceed 10^{16} J.

Let us now turn to the electrical current produced by the ring-current particles. The foregoing procedure implies that we can add up the contributions of each gyrating and drifting particle to get the effect of the entire ring current. This can be done, but the procedure is rather delicate because the varying particle density makes it difficult to calculate properly the contributions from individual orbits. These effects are illustrated in Fig. 3. First, consider particles gyrating in a uniform magnetic field (Fig. 3a) with the particle density and pressure increasing to the right (as indicated by the relative thickness of the orbits). The net effect at the tangency of their orbits is to produce a current toward the top of the page. Thus, a pressure gradient produces a particle current, even if the magnetic field is homogeneous. If, on the other hand, the field is nonhomogeneous (Fig. 3b), then not only are there gradient and curvature drifts (since gradient and curvature always occur together in the absence of a local current), but the orbits bunch together on the concave sides of the field lines, modifying those currents.

There is a more straightforward way to arrive at the current, based on a simple physical argument. Any assemblage of particles exerts a pressure, represented in general by a pressure tensor **P**. The total force required to confine the particles is $-\nabla \cdot \mathbf{P}$. In a steady-state collisionless plasma, this confinement force is provided by

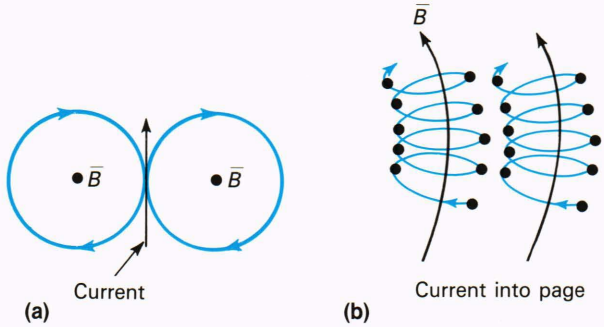

Figure 3 — (a) How current is produced by the particle pressure gradient. Particle intensity is indicated by the darkness of the gyration circles. A positive gradient (intensity increasing away from the earth) leads to an eastward current. (b) The eastward current between the two curved field lines is produced by the crowding of gyro orbits on the concave side of the lines.

the Lorentz force $\bar{\imath} \times \bar{B}$ (where $\bar{\imath}$ is the electrical current density in amperes per square meter), which may be calculated from

$$\bar{\imath} \times \bar{B} = -\nabla \cdot \mathbf{P} \ . \qquad (7)$$

Figure 4 illustrates the concept.

The pressure tensor for a magnetized gyrotropic plasma is diagonal, with scalar pressures $P_\perp$ and $P_\parallel$ (perpendicular and parallel to the field lines, respectively), calculated from

$$P_\perp = \int f(\bar{v}) E \sin^2\alpha \, d^3v \qquad (8)$$

and

$$P_\parallel = 2\int f(\bar{v}) \, E \cos^2\alpha \, d^3v \ , \qquad (9)$$

where α again is the particle pitch angle defined in Eq. 1, $\bar{v}$ is the velocity, and $f(\bar{v})$ is the phase-space density for the particles. If several particle species are present, the contribution of each species to $P_\parallel$ and $P_\perp$ must be calculated separately and then summed to give the total pressure tensor. Likewise, $\bar{\imath}$ is the total electrical current density caused by all charged species.

The force $-\nabla \cdot \mathbf{P}$ can be calculated using Maxwell's equations, $\nabla \cdot \bar{B} = 0$ and $\nabla \times \bar{B} = \mu_0 \bar{\imath}$. Taking the cross product of $\nabla \cdot \mathbf{P}$ with $\bar{B}$ in Eq. 7, we obtain the electrical current perpendicular to the field from the identity $\bar{B} \times (\bar{\imath} \times \bar{B}) \equiv B^2 \bar{\imath}_\perp$:

$$\bar{\imath}_\perp = \bar{B} \times [\nabla P_\perp + (\delta P/B)\hat{B} \cdot \nabla \hat{B}]/B^2 \ , \qquad (10)$$

where $\delta P = P_\parallel - P_\perp$. Parker[9] obtained this result by summing the contributions of individual particle motions over the entire particle distribution. From Maxwell's equation, $\nabla \times \bar{B} = \mu_0 \bar{\imath}$, it is possible to express $\bar{\imath}_\perp$ independently of particle pressure terms and solely in terms of the transverse components of both the field curvature ($\hat{B} \cdot \nabla \hat{B}$) and gradient ($\nabla B$). Applying cross products with B twice to $\bar{\imath}$ (as above) and using the identity $B\nabla B \equiv \bar{B} \times (\nabla \times \bar{B}) + \bar{B} \cdot \nabla \bar{B}$, we have

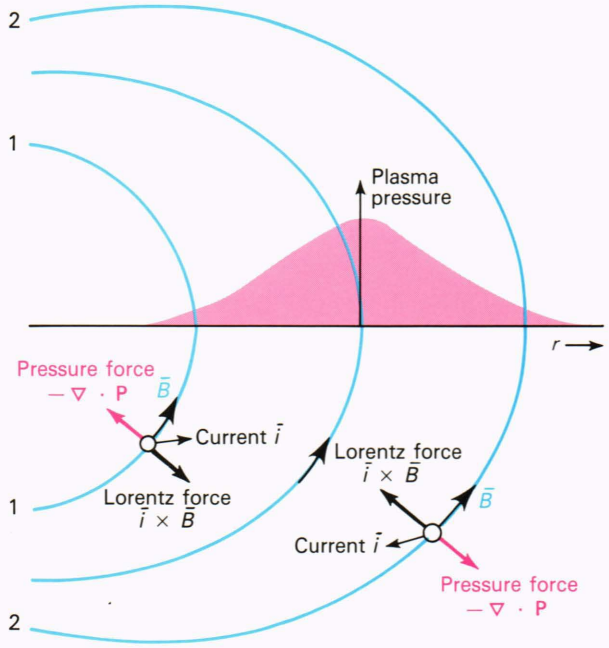

Figure 4 — The magnetic confinement of a hot plasma. The pressure force $-\nabla \cdot \mathbf{P}$ must be balanced by the Lorentz force $\bar{i} \times \bar{B}$, so electric current must flow.

$$\mu_0 \bar{i}_\perp = -\hat{B} \times (\hat{B} \times \mu_0 \bar{i})$$
$$= -\hat{B} \times (\hat{B} \times \nabla \times \hat{B})$$
$$= \bar{B} \times (\hat{B} \cdot \nabla \hat{B}) - \hat{B} \times \nabla B \ . \quad (11)$$

Using Eq. 11, we can replace the curvature term in Eq. 10 with a term involving ∇B and $\bar{i}_\perp$. Thus, whenever the curvature vector is difficult to estimate quantitatively (for example, from equatorial single spacecraft observations), an alternative expression given by Vasyliunas[24] in which only ∇B appears can be used:

$$\bar{i}_\perp = \bar{B} \times [\nabla P_\perp + (\delta P/B) \nabla B]/(B^2 - \mu_0 \delta P) \ . \quad (12)$$

There is no information in the force-balance relation (Eq. 7) about the field-aligned component of the current $\bar{i}_\parallel = i_\parallel \hat{B}$. That must be obtained from Kirchhoff's law, $\nabla \cdot \bar{i} = 0$ (assuming no charge accumulation in a quasi-steady state). Since $\nabla \cdot (\bar{i}_\parallel) = \bar{B} \cdot \nabla (i_\parallel / B)$, we obtain a differential equation for $i_\parallel$:

$$(\partial / \partial s)(i_\parallel / B) = -(1/B) \nabla \cdot \bar{i}_\perp \ , \quad (13)$$

which may be integrated with respect to s, the distance along a field line.

Because of charge neutrality, the ion species dominate the pressure tensor when the electrons are "colder" than the ions. Thus, the ion population drives $\bar{i}_\perp$ in the inner magnetosphere. On the other hand, the higher mobility of the electrons makes them the prime candidates for carrying the field-aligned currents, $\bar{i}_\parallel$. One might therefore think that both electron and ion populations would have to be measured to understand the dynamics of the full set of electrical currents. Equations 10 or 11 and 13 reveal, however, that both $\bar{i}_\perp$ and $\bar{i}_\parallel$ are determined by the ion pressure tensor (assuming that the actual magnetic field is known to sufficient approximation). As we shall see, the pressure tensor can be derived globally from ENA images, which is why ENA imaging offers such a powerful tool for research into magnetospheric dynamics.

IN SITU MEASUREMENTS OF THE RING CURRENT

Early Measurements

Since Eq. 6 shows that the magnetic field perturbation at the earth's surface is proportional to the total kinetic energy of the particle population, it is appropriate to consider the ring current in the perspective of energy density. Figure 5a shows plots of ring-current energy density versus altitude obtained from NASA's Explorer 45 satellite during the 17 December 1971 magnetic storm.[17] The energy density calculation assumes that the measured ions are protons and has been carried out over the energy range of 1 to 138 keV. Orbit 97 shows prestorm levels, orbit 101 shows the asymmetric main-phase development, and orbits 102 and 103 show the storm recovery phase. The data are plotted as a function of L value, where L is the radial distance (in earth radii) to the equatorial crossing point of the magnetic field line through the spacecraft.

Of interest in Fig. 5a are the pressure gradients during the storm. The steep decrease at low altitudes represents an eastward current (see Fig. 4), which is opposite to the westward current required for the observed magnetic field decrease at the earth's surface shown in Fig. 1b. The steady decrease toward high altitudes, however, gives a westward current and, since the pressure gradient term is weighted by $B^{-1} \propto R^3$ (Eq. 10), it is this portion of the particle distribution that will provide the current causing the observed surface field depression. Note that the longitudinal asymmetry indicated during the main phase of the storm (orbit 101 in Fig. 5a) will give rise to a radial current system (Eq. 10), which, for strong asymmetries, may play an important role in ring-current dynamics. Such radial currents generally have been overlooked in the literature and are only now being studied in detail.[25,26]

For the same magnetic storm, Fig. 5b shows the measured differential energy density of the ring current. The solid data points (orbit 102) were obtained in the storm recovery phase and at the altitude (approximately 3.6 R_e) of maximum ring-current intensity. A prestorm plot of the quiet-time energy density (orbit 97) is shown for comparison. Similar results both in relative changes during the storm and in absolute energy densities observed have been reported for a magnetic storm in November 1977.[27] Figure 5b indicates that the main injection of ring-current particles is at energies $\lesssim 200$ keV, whereas particles at energies $\gtrsim 200$ keV show a decrease in intensity. This result is because of an adiabatic re-

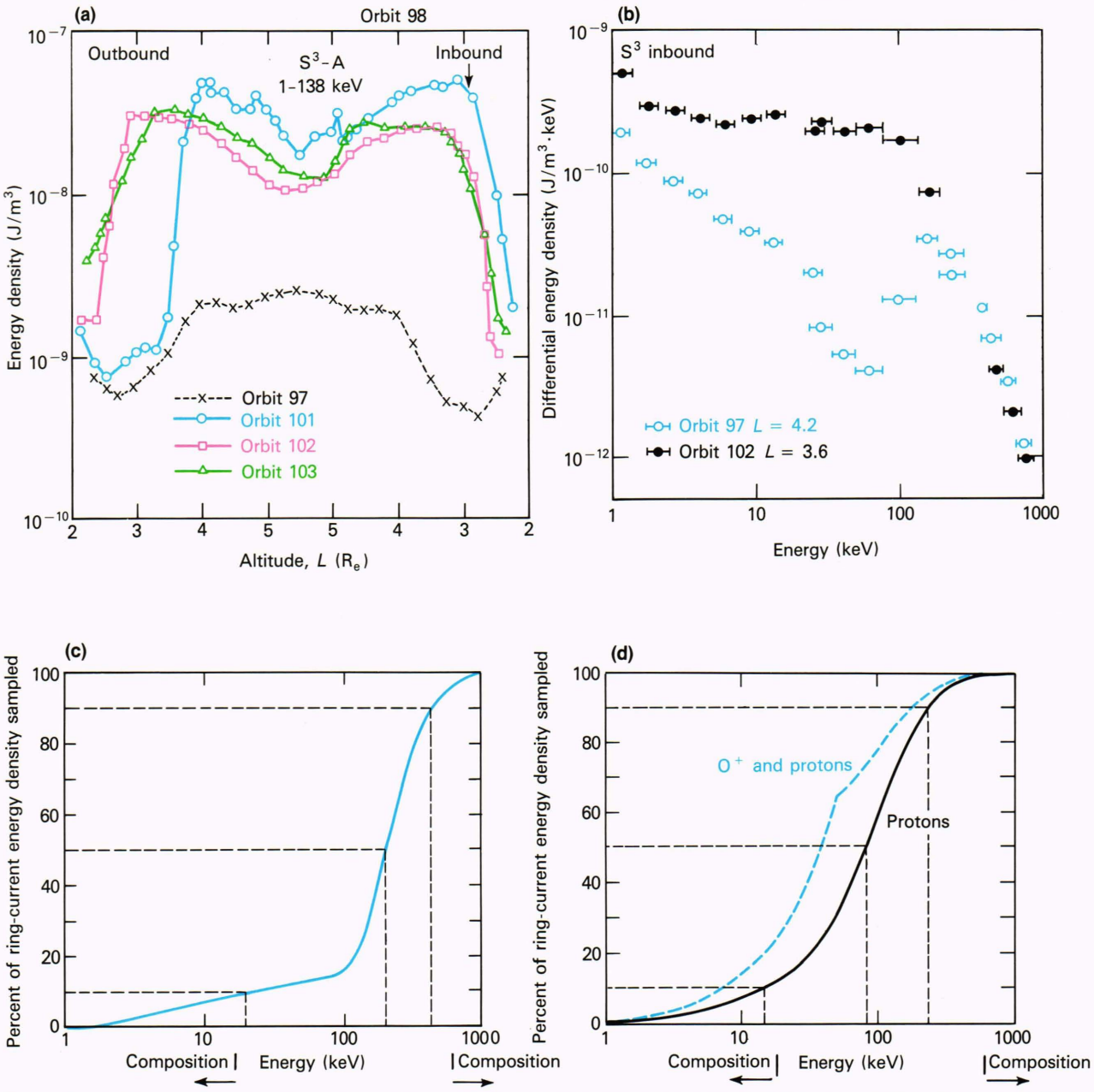

Figure 5 — (a) Proton energy-density radial profiles as measured for the magnetic storm of 17 December 1971 by Explorer 45 (S^3-A) during the prestorm quiet (orbit 97), main-phase injection (orbit 101), and recovery phase (orbits 102 and 103).[17] (b) Ion energy-density spectra (protons assumed) measured by Explorer 45 during prestorm quiet (orbit 97) and recovery phase (orbit 102) for the 17 December 1971 magnetic storm.[17] (c) The accumulated percentage of ring-current energy density versus energy calculated from data in Fig. 5b for prestorm quiet period. Energy ranges of the then-available direct composition measurements[19,28] are indicated. (d) Same as Fig. 5c, for the recovery phase. The solid curve assumes all ions are protons; the dashed curve assumes all ions are O^+ below 50 keV and all are protons above 50 keV.

sponse of the energetic particles to the new magnetic field configuration caused by the low-energy particle injection (the ring current).

Integration of the curves of Fig. 5b over energy yields the results shown in Figs. 5c and 5d,[19,28] where the accumulated percentage of ring-current energy density is plotted against energy. Quiet time and recovery phase are shown. The recovery-phase solid curve assumes the ring-current particles are all protons; the dashed curve assumes all O^+ ions below 50 keV and all protons above 50 keV. Assuming protons, the median energy in the integral energy-density curve is approximately 85 keV. Energies for which composition measurements have been made in the magnetosphere (before observations made by the recent APL CCE)[6] are indicated by the lines at approximately 17 and 550 keV.

Figures 5c and 5d show that, although we have known the energy range of the ring-current particles for many years, we have not had composition observations for the bulk (80 to 90%) of these particles before the CCE ob-

servations. This has effectively prevented us from identifying the source of the ring-current particles. The low-energy tail ($\lesssim 20$ keV) of the ring-current distribution has been thought to have an ionospheric origin, whereas the high-energy tail ($\gtrsim 600$ keV) has been thought to have a solar-wind origin. How, or if, these two sources mix to produce the bulk ring current was unknown.

Recent Measurements

The situation regarding observations of ring-current composition has changed. The CCE was launched in August 1984 as part of the joint three-satellite AMPTE program conducted by the United States, the Federal Republic of Germany, and the United Kingdom. A major objective of the AMPTE program was the release of gases into the solar wind and distant geomagnetic tail, and the observation of the entry and transport of the resulting ions to the lower magnetosphere. To perform the latter observations, the CCE was placed in an elliptical, nearly equatorial orbit with an apogee of 8.8 R_e and a period of 15.7 h. It carried into space the first comprehensive set of composition and charge-state instrumentation that could span the entire ring-current energy range. Initial CCE ring-current results for the 4 September 1984 magnetic storm were recently published in a set of seven papers.[4] Although these results are preliminary and pertain to just one magnetic storm, they are exciting and hold high promise for solving several long-standing ring-current problems. A more thorough analysis of the CCE observations of the ring current in this storm, as well as in another storm (18–20 September 1984), has recently been published by Lui et al.[29] Three points are worth noting: neither storm was large ($D_{st} > -120$ nT and $D_{st} > -60$ nT, respectively); in both storms the CCE orbit lay mainly in the early afternoon sector; and the observations occurred at solar minimum. Evidence is accumulating, primarily from ENA observations (see the ENA section below), that in large storms nearer solar maximum the largest ion fluxes appear in the midnight sector. Also, *in situ* measurements by Young et al.[30] have established that O^+ has a higher abundance (relative to H^+) in the magnetosphere at solar maximum. Bearing these points in mind, we briefly highlight the CCE results in the following paragraphs.

Figure 6 shows measured oxygen charge states summed over an inbound pass on 5 September 1984 during the magnetic storm.[31] The two source regions are identified by the two charge-state groups; high charge states are associated with the solar wind, low charge states with the ionosphere. Whereas Fig. 6 shows a dominant ionospheric oxygen source as summed over L values of 8.6 to 2.3 R_e, Fig. 7 shows that protons dominated the ring-current energy density at all altitudes over the energy-per-charge range of 5.2 to 315 keV/q. It can also be seen that the relative strength of the ionospheric source decreases (with respect to the solar-wind source) with increasing altitude.

One of the main results from the 4 September 1984 storm was the observation that protons were the dominant ions throughout the bulk of the ring current. A combination of all CCE particle data[32] shows that (1) the prestorm ring current consisted primarily of protons and was peaked in energy at approximately 200 keV (as indicated in Fig. 5); (2) the main ring-current intensity enhancement occurred in the approximately 20- to 200-keV range; and (3) protons with energies $\gtrsim 50$ keV dominated the storm-time ring-current energy density, with oxygen ions contributing approximately 27%. These last two results are summarized in Fig. 8, where we show the accumulated percentage of total ring-current energy density as a function of energy obtained at $L = 3.9$ of the radial profiles shown in Fig. 7. The data for the various species are as presented by Stüdemann et al.;[33] we have added a curve summing the contributions of all ions. Note that a logarithmic scale is used below 1% in Fig. 8 to highlight the contributions of He^+, He^{2+}, and O^{2+}. Both the curve for all ions in Fig. 8 and the S^3 energy density curve in Fig. 5d show the same general result: that from the perspective of energy density, the ring-current mean energy is several tens of kiloelec-

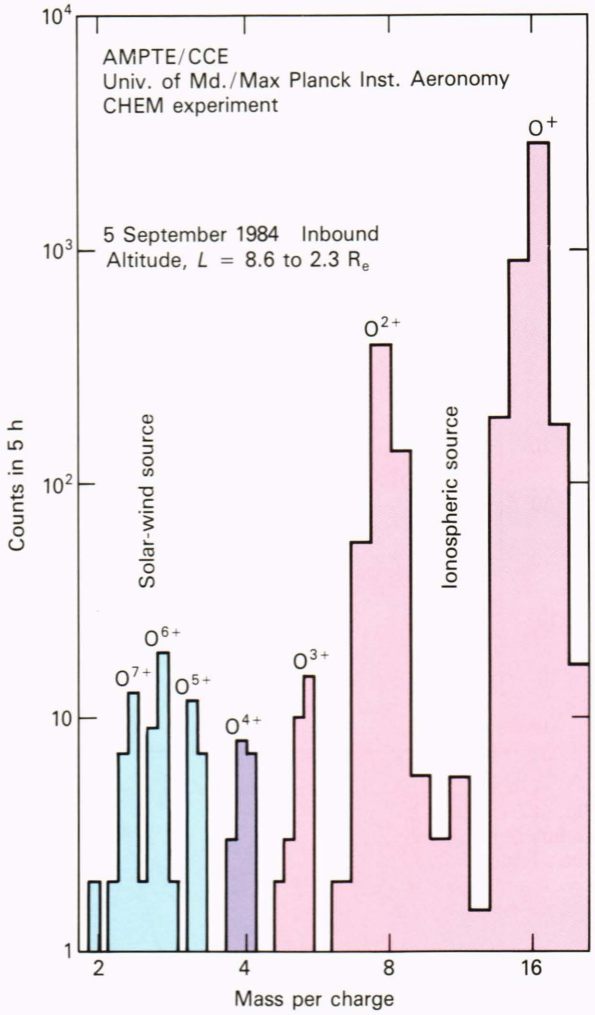

Figure 6 — Charge-state histogram of approximately 1 to 300 keV/q oxygen in the earth's ring current during the geomagnetic storm of 4–7 September 1984. Contributions from the ionosphere ($O^{+1,2}$), the solar wind ($O^{+6,7}$), and from charge exchange ($O^{+3,4,5}$) are evident.[31]

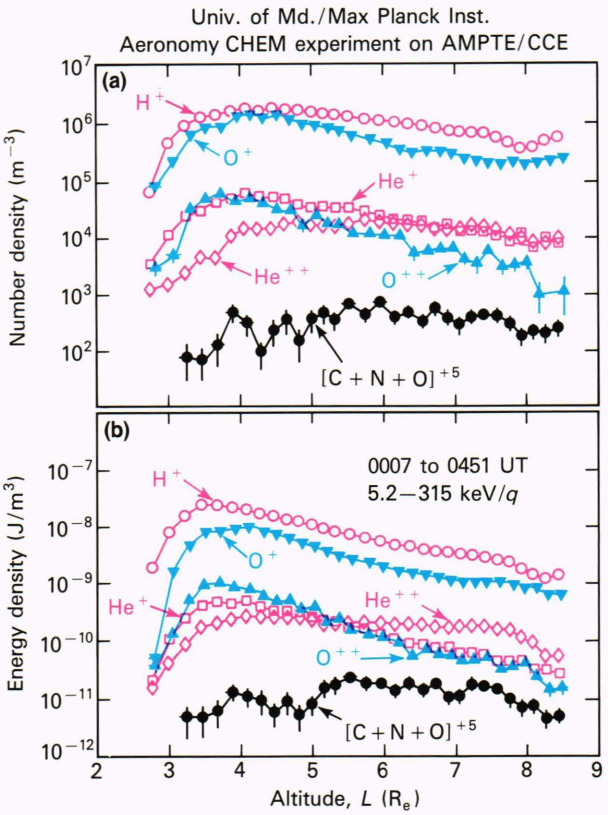

Figure 7 — Radial profiles of (a) the number density and (b) the energy density during the inbound pass on 5 September 1984. The *e*-folding values for the number (energy) densities between L = 4 and 6.5 R_e are 3.3 (1.5), 1.7 (1.3), 1.2(1.0), and 2.0(1.5) for 5 to 31 keV/q H^+, O^+, O^{++}, and He^+, respectively.[31]

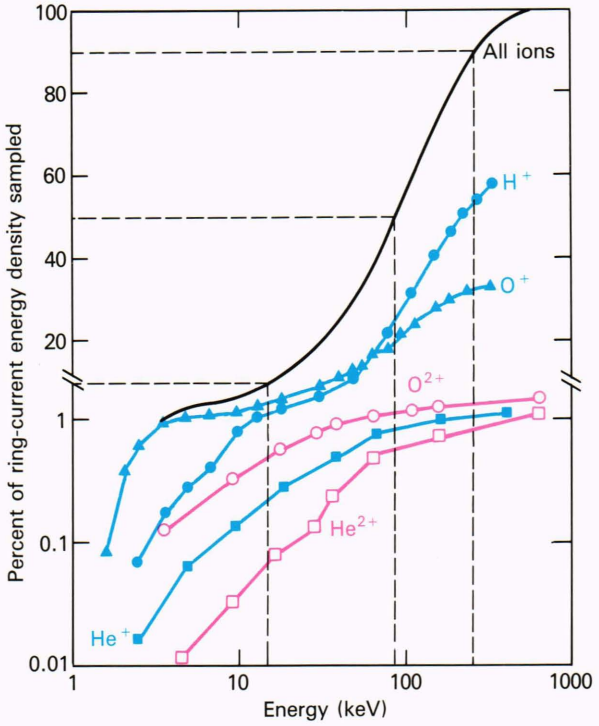

Figure 8 — The accumulated percentage of ring-current energy density versus energy, adapted from data presented in Ref. 33 obtained at L = 3.9 R_e during the 5 September 1984 CCE pass shown in Fig. 7. A logarithmic scale is used below the 1% level. The total energy density curve (all ions) is similar to that of the December 1971 storm (Fig. 5d).

tronvolts (approximately 85 keV) and that the bulk (approximately 90%) of the ring current is contained in the 15- to 250-keV energy range.

Locating the Currents

To locate the region of the main current flow, Lui et al.[29] used the data of McEntire et al.[34] to calculate the magnitude of the ring current as a function of radial distance, according to Eq. 10. The data used are for total ions with energies $\gtrsim$25 keV; it has been assumed that protons constitute the primary contributor to the pressure terms at those energies. The results are shown in Fig. 9. In the upper panel, $P_\perp$ is shown as a function of radial distance for both a prestorm pass and the storm-time pass occurring on 4–5 September 1985. The bottom panel shows the resulting total current for the two passes, as well as the current caused by the pressure anisotropy term in Eq. 10. We see that the total current is dominated by the pressure gradient term, resulting in an eastward current at the inner edge of the ring-current distribution and an extended westward current caused by the pressure gradient at altitudes higher than the pressure peak. Integrating the current in Fig. 9 over radial distance, estimating a latitudinal ring-current thickness from pitch-angle observations, and assuming a symmetric ring-current model yields an expected D_{st} value in agreement with that which occurred during the time of the pass (approximately −60 nT). That may be only a fortuitous agreement, since a local measurement of the ring-current particle population tells little about the global distribution of the current. For example, the assumption of a symmetric ring current implies that there are no radial currents. As we have discussed, radial currents may be important in the dynamics of the ring-current system.

Composition: The Solar Wind and Ionosphere as Sources

Ionosphere and solar-wind source mixing is another example of a problem that is being studied with the CCE data. The ion charge-state measurements should uniquely identify the source regions and their relative strengths. For example, we show in Fig. 10 a sample of results obtained from initial studies of charge-state distributions.[35,36] The figure shows observed oxygen charge states for three separate altitude ranges during two time periods representing different local times. Similar data were also obtained for the charge states of carbon. Since the instrument geometric factor has not been folded into the data of Fig. 10, those data show only relative charge-state changes with altitude. The data are from periods of low to moderate magnetic activity.

The data in Fig. 10 indicate, in a qualitative sense, that the relative strengths of the ionospheric and solar-wind sources change with radial distance in the manner expected, with the solar-wind source increasing in

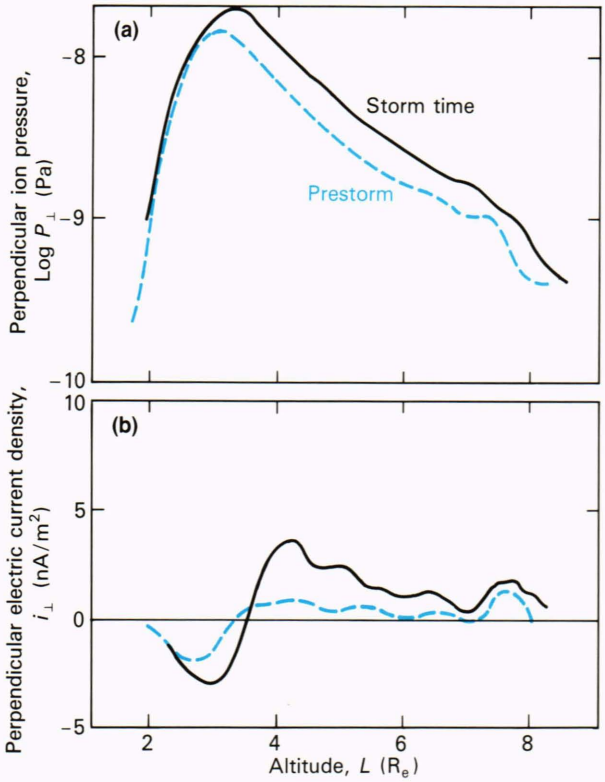

Figure 9 — Calculation of (a) perpendicular pressure $P_\perp$ and (b) resulting current $i_\perp$ for the total ion distribution (assumed protons) above 25 keV for the magnetic storm of 4–5 September 1984 (see Eq. 10). The dashed line shows a prestorm CCE pass and the solid line shows a storm-time pass. Currents are localized where the pressure gradient is large.

strength as radius increases. This trend seems clear during both time periods if we identify the low charge states (O^+, O^{2+}) with an ionospheric source and the high charge states (O^{5+}, O^{6+}, O^{7+}) with a solar-wind source. The very existence of such high and low charge-state peaks, and their spatial evolution (also observed in carbon data) clearly show, however, both a solar-wind and an ionospheric component to the magnetospheric particle population. To quantify the absolute charge-state intensities and assign them to a source population will require an accounting of charge exchange, diffusion, and drift trajectory effects. For example, in Fig. 10, the lack of significant high charge-state intensities at low altitudes does not necessarily indicate the absence of solar-wind particles, but instead may indicate that solar-wind oxygen has reached an equilibrium charge distribution in which no high charge states remain.[37] These factors and the large intensity variations between the two time periods in Fig. 10 show that we should not expect the same ionosphere/solar-wind mixing ratio through the magnetosphere for all magnetic storms. It would change from storm to storm, depending on the past history of magnetospheric activity.

Measurements of molecular ions in the magnetosphere provide a new tool with which to study the acceleration of ionospheric plasma. Upflowing fluxes of N_2^+, NO^+, and O_2^+ up to energies of 20 eV have been measured at radial distances of approximately 1.1 to 2.5 R_e over the polar caps during a magnetic storm.[38] Energetic (80 to 230 keV) O_2^+ and NO^+ were observed in the outer ring current ($6.6 \lesssim L \lesssim 8.3$) during the 4 September 1984 geomagnetic storm.[39] These observations, showing the large intrinsic accelerating capabilities of the magnetosphere, should provide an important additional key to help unravel the various ring-current generation processes described below.

Although many more magnetic storms must be analyzed before a comprehensive picture of ring-current sources, energization, and generation will emerge, the early CCE results presented here demonstrate a new capacity for solving these long-standing space plasma physics problems connected with ring-current formation.

RING-CURRENT GENERATION

We now briefly discuss various ring-current generation mechanisms that have been advanced over the years and try to interrelate them within a unified picture of the generation process.

Earthward Convection of the Plasma Sheet

In this case, an enhanced dawn–dusk electric field quickly convects the plasma sheet particles toward the earth on the nightside hemisphere via $\bar{E} \times \bar{B}$ drifts. The convected particles experience betatron and Fermi accelerations as they are transported to small radial distances (approximately 2.5 to 4.0 R_e) by the enhanced field to form the ring current (see, for example, the discussions by Frank[16] and Axford[40]).

Acceleration of Ionospheric Ions by Electric Fields Parallel to Auroral Field Lines

Since the time when energetic ($\lesssim$10 keV) ion beams were first observed streaming out of the ionosphere in auroral regions,[41] it has been attractive to consider such particles as a source for the ring current. Additional mechanisms are required to form the normally observed equatorial pitch-angle distributions ($\sin^n\alpha$, $n \geq 0$), which would then be displaced to low altitude by an enhanced dawn–dusk electric field and accelerated to ring-current energies by betatron and Fermi processes.

Acceleration at a Source Boundary

To explain the complex energy–time signature displayed by energetic ($\lesssim$30 keV) particles at geostationary orbit, McIlwain[42] suggested that enhanced electric fields cause the appearance of fresh energetic particles at locations outside a sharp, well-defined boundary in the nightside hemisphere. After the transient, enhanced electric field, the particles move in the ambient, quiescent magnetic–electric field configuration. Using a realistic magnetic field and an electric field model inferred from particle data, McIlwain was able to explain many of the particle energy–time signatures observed at geostationary altitudes. His hypothesis has been successfully tested.[43-45] Particle observations in the dusk–midnight sector also are consistent with particle motion in the existing magnetic and electric field configuration.[46-48] Midnight–dawn sector observations and observations of zones apparently in-

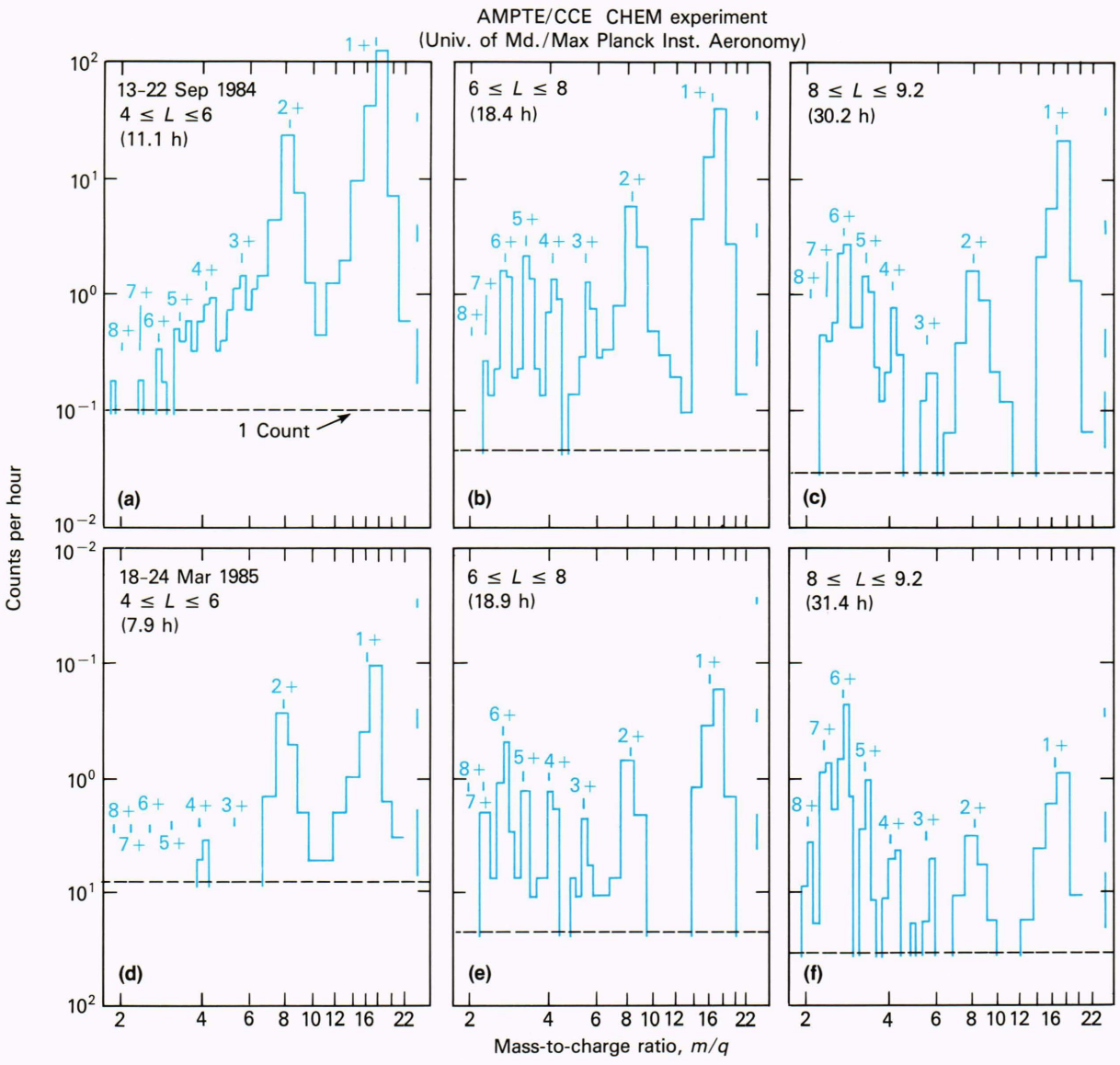

Figure 10 — Charge-state distributions of oxygen for three ranges of *L* and two different local times: a, b, and c, 1300 LT; d, e, and f, 0300 LT. Characteristic error bars are plotted on the right side of each panel. The numbers in parentheses represent the accumulation times for the data. Identifying the high charge-state peak with a solar-wind source and the low charge-state peak with an ionospheric wind source reveals how these two sources mix as a function of altitude.[35]

accessible to particles offer further evidence supporting the source boundary concept.[49,50]

Inward Motion of the Outer Radiation Zone

The enhanced electric field responsible for rapid convection of the plasma sheet toward the earth will also cause an inward motion of previously trapped particles in the earth's outer radiation zone. Lyons and Williams[51] quantitatively tested this concept using data from two main-phase magnetic storms in 1971 and 1972. They found that the main-phase ring current could be accounted for by the inward motion of trapped particles from the prestorm outer zone. In their model the outer zone was populated by continuing injection events. The appearance of both ions and electrons in the ring current is consistent with this hypothesis. The same mechanism was invoked successfully to explain energetic (>137 keV) oxygen increases in the 4–5 September 1985 storm-time ring current.[52]

The interrelated mechanisms discussed above can be unified by considering a two-step process for ring-current formation. The basic idea is as discussed above[51] and recently considered in more detail by Mauk and Meng:[53] (1) the outer radiation belt regions ($\gtrsim 5$ R_e) are kept populated by a continuing series of injection events and (2) the storm-time ring current (approximately 2.5 to 5 R_e) is formed by enhanced dawn–dusk electric fields convecting the outer trapped particle populations inward. Thus, the first three mechanisms discussed in this section can keep the outer zone populated and the fourth can form the ring current. Mauk and Meng[53]

argue for this two-step process and use the third mechanism as the source of the injection events, observed at geostationary altitudes, that keep the outer radiation belts populated. Diffusion across magnetic field lines then populates the inner trapping regions, and enhanced dawn–dusk electric fields form the storm-time ring current.

RING-CURRENT DECAY

Charge exchange has long been considered a major loss mechanism for ring-current particles.[11,54-56] The process is summarized in Fig. 11. The ring-current region is permeated by a tenuous cloud of relatively cold (1000 K) hydrogen atoms. The atoms are the lightest constitutents of the outer atmosphere (the exosphere), and they boil off in ballistic orbits, some of which are converted to Keplerian trapped or escaping orbits by collisions with other H atoms. This outwardly decreasing cloud resonantly scatters solar Lyman-alpha photons, producing a faint glow around the earth called the "geocorona." The H atoms themselves are therefore called the hydrogen geocorona. Recently, Rairden et al.[57] used their ultraviolet measurements from the DE 1 spacecraft to deduce the hydrogen geocorona density from their Lyman-alpha measurements. The approximate radial dependence of the geocoronal H-atom density n_H is shown in the upper left of Fig. 11.

The energetic trapped ions in the ring-current region will occasionally experience a charge-exchange collision with a cold geocoronal H atom in which the energetic ion acquires the electron of the H atom. Since most of the energetic ions in the storm-time ring current are singly charged (see the previous section on composition), they become energetic neutral atoms (ENA) after charge-exchange, as shown in the lower right of Fig. 11. Because only a few electronvolts of energy are lost in the charge-exchange collision, the energetic ion, now transformed into an ENA, retains both the energy and direction it had at the moment of neutralization. With a velocity

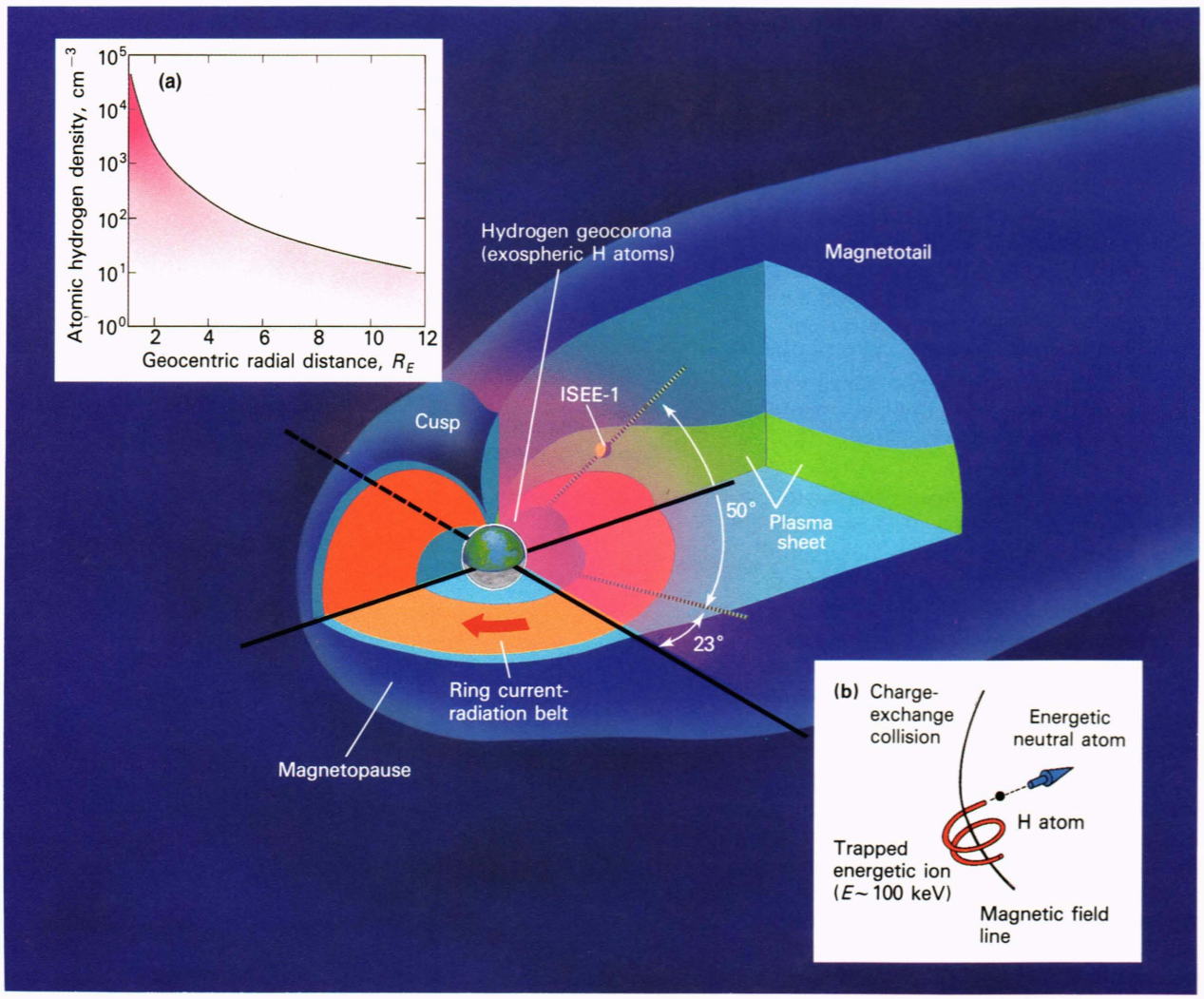

Figure 11 — The production of ENA in the magnetospheric regions depicted in Fig. 1a. Insert a: The radial dependence of exospheric hydrogen atom density. Insert b: Charge-exchange collision with exospheric hydrogen atom that converts energetic ions into ENA.

of several thousand kilometers per second, gravitational effects are negligible, and the ENA escapes the magnetosphere along a straight line, in a manner similar to that of a photon. Such charge-exchange collisions are rare (about one every 7 hours for a 25-keV proton at an equatorial radius r of 3.5 R_e); the intensification of the ions during magnetic storms can produce ENA fluxes greater than $10^7/m^2 \cdot s \cdot sr \cdot keV$ at these energies.

Previously, the lack of ring-current composition data, together with uncertainty in the energy- and species-dependence of charge-exchange cross sections, hampered attempts to check quantitatively the role of charge-exchange in ring-current decay. Its importance as a ring-current loss mechanism has been inferred indirectly, however. For example, Smith et al.[58] performed a best-fit analysis of charge-exchange loss to the observed decay in low-energy ion population of the ring current. No direct composition measurements were available. The parameters extracted from the decay curves at various energies were the relative abundance and charge-exchange lifetimes of each ion species. The lifetimes obtained from this analysis were the charge-exchange lifetimes of H^+, He^+, and O^+, which showed that a multispecies ring current in a charge-exchange analysis could account for the total ion population decay times obtained from *in situ* measurements.

But charge exchange is not the sole dissipative mechanism operating on the ring current. Cornwall et al.[59] predicted intense turbulence caused by ion cyclotron waves generated by the interaction of the ring-current particles with the cold plasma in the plasmasphere. The resulting pitch-angle diffusion into the atmosphere of the ring-current particles would represent a major loss process at the inner edge of the ring current. Williams and Lyons[60,61] showed that the pitch-angle evolution of ring-current particles in the plasmapause region was consistent with the generation of ion cyclotron waves, although wave growth and resulting particle loss was not nearly as strong as predicted.

Even though ring-current pitch-angle diffusion was weak instead of strong, sufficient energy may be lost from the ring current to cause observable atmospheric effects. By integrating the energy lost from the ring current as a result of changes in the pitch-angle distribution observed in the plasmapause region, Williams et al.[62] estimated the energy deposition into the ionosphere as a function of L value (the equatorial crossing distance of an earth dipole field line). A comparison of their results with double subauroral red arc structures that were simultaneously observed in the ionosphere showed that the energy lost from the ring current was sufficient to sustain the observed arcs, a result consistent with the theoretical prediction.[63] Further, the equatorial location of the two high-altitude peaks in the ring-current loss were consistent with the observed arc positions when the ring-current-inflated magnetic field was taken into account.

We see, then, that ring-current decay is due primarily to charge exchange, but there is weak pitch-angle scattering occurring at the inner edge of the ring current, as well. The pitch-angle scattering is sufficient to cause observable atmospheric effects.

ENA: IMAGING THE RING CURRENT

The very charge-exchange process that depletes the ring current of energetic ions also provides the means of imaging the ring current. As we mentioned earlier, the ENA fly off in straight lines, retaining the velocity that the energetic ion had just before the charge-exchange collision. The exact relation between the unidirectional differential fluxes of the ENA (j_{ena}) and the ions (j_{ion}) that produced them is given by a line integral along the line of sight from the detector to infinity:

$$j_{ena} = \sigma(E) \int_0^\infty dl \, n_H \, j_{ion} \, , \qquad (14)$$

where $\sigma(E)$ is the charge-exchange cross section in square meters, dl is an increment of path length (in meters), n_H is the geocoronal H-atom density, and j_{ion} is evaluated at the pitch angle corresponding to the line of sight directed toward the detector. The charge-exchange cross sections[64] for the two most populous ions in the storm-time ring current (H^+ and O^+) are shown in Fig. 12, where one immediately sees that ENA measurements are significantly more sensitive to O^+ ions than to H^+ ions for energies greater than 50 keV.

To demonstrate the amount of global information contained in ENA images, we have formulated a model

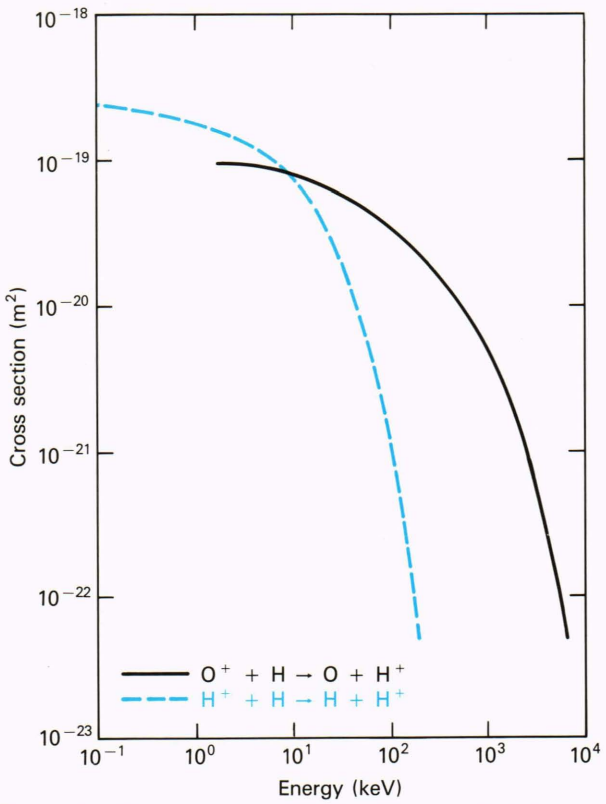

Figure 12 — Energy dependence of the cross section for charge exchange of H^+ and O^+ energetic ions on H atoms.[64]

approximating the two-stage injection/energization process described in the preceding section on storm-time ring-current generation. Figures 13a through 13c illustrate the evolution of the spatial distribution (in the magnetic equatorial plane) of a given species of ring-current ions. In Fig. 13a the ions start at an injection boundary concentrated in the midnight sector at 5.5 to 6.0 R_e. The enhanced cross-tail electric field then drives the injected population inward (Fig. 13b). Magnetic field gradient and curvature drifts cause the ions in this injection population to follow trajectories through the evening hours, past noon, and into the early morning hours, thereby finally establishing, as shown in Fig. 13c, an asymmetric, early-recovery-phase population with a weak (2:1) midnight-to-noon asymmetry. An evolving pitch-angle distribution, chosen to represent an evolving ion pressure tensor, is shown in panels 13d to 13f for times t_1, t_2, and t_3, corresponding to panels 13a to 13c.

We next compute the ENA image from Eq. 14, using the H-atom geocoronal density function obtained from the DE 1 spacecraft, as shown in Fig. 11. We place the simulated viewing point at 8 R_e and 30°N geomagnetic latitude on the dusk meridian. Figures 14a to 14c present the ion-flux column intensities logarithmically (in false color), corresponding to the spatial distributions shown in Figs. 13a to 13c. A range of intensity spanning a factor of 1000, normalized to the maximum intensity, is given in each panel. The ion-flux column intensities provide a line-of-sight measure of the ring-current ions obtained by carrying out the integral in Eq. 14 without the factor n_H under the integral or the multiplicative factor $\sigma(E)$. The pitch-angle dependence is therefore folded into the integral. Contours of the inner and outer L-shells bounding the ion population (see Fig. 13) are shown in Figs. 14b and 14c. These contours are connected in the magnetic equatorial plane by lines of constant magnetic local time (MLT) drawn for every 3 hours. The storm-time magnetic field lines have been compressed on the dayside and extended on the nightside, as shown in Fig. 13. Figures 14d to 14f show the ENA fluxes as computed from Eq. 14, again normalized to the maximum flux in each panel.

AN ENA IMAGE FROM ISEE-1

The foregoing discussion is based on a semiquantitative model summarizing our ideas on the generation of the ring current as it might appear when viewed in ENA emission. Let us now turn to actual ENA measurements of the storm-time ring current. Although observational constraints have not yet allowed us to construct a complete time history of a single storm, the ENA images obtained to date confirm the general concept of injection in the midnight sector and a nonaxisymmetric ring current during the main phase.

ENA images have been obtained using the medium-energy particle instrument (MEPI) on the ISEE-1 spacecraft.[65] The MEPI contains a narrowly collimated (5° half-angle) energetic-particle telescope with a set of solid-state detectors. A magnet focuses energetic electrons off-axis onto one set of detectors, while the more massive

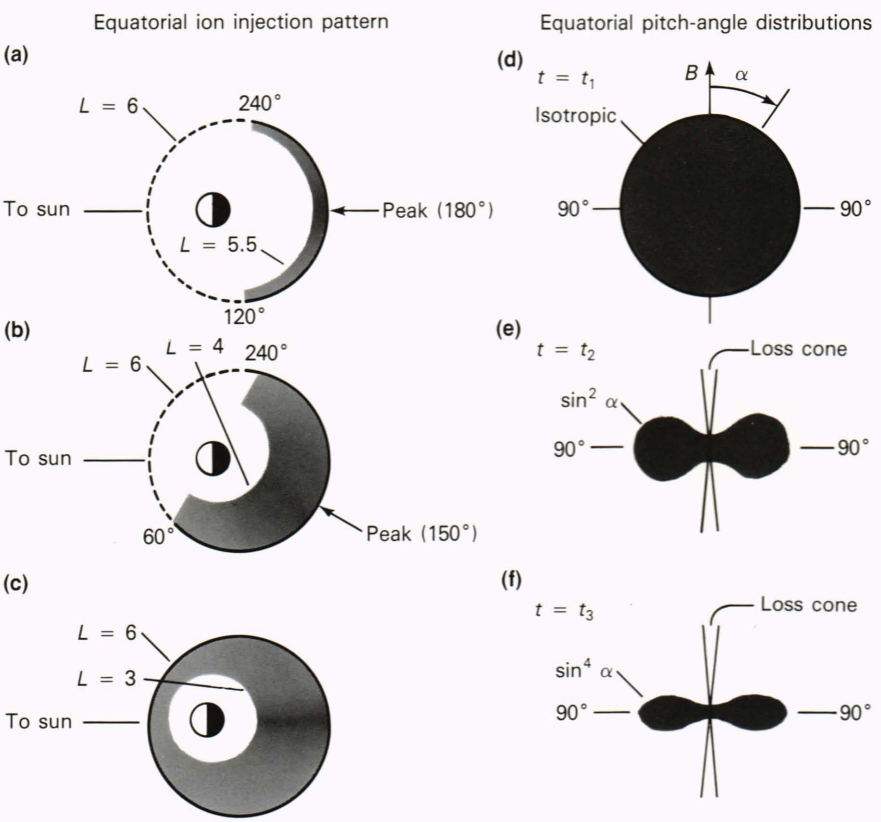

Figure 13 — Schematic of modeled ring-current injection-ion density evolution as a function of time: (a to c) equatorial spatial evolution; (d to f) ion pitch-angle distribution evolution.

ions of energies greater than 25 keV impinge on a "straight-through" detector. A motor sweeps the telescope from ecliptic north to ecliptic south as the spacecraft spins about a north–south axis in 3 s. It takes 12 spins for the motor to scan north-to-south and another 12 spins to scan south-to-north; thus, the MEPI scans the entire sky every 36 s.

The MEPI will respond to energetic neutral atoms as well as ions with energies greater than 25 keV. The ISEE-1 orbit occasionally places the spacecraft on open, polar magnetic field lines as close as $r = 2.6\ R_e$ at geomagnetic latitudes above 50°. On open field lines, the trapped-ion fluxes drop to negligible levels, and if the ring current is energized by a magnetic storm at the time, the MEPI can count ENA. Consequently, the MEPI, with its all-sky coverage, can synthesize an image of the singly charged energetic ions in the ring current, using the hydrogen geocorona as a converter.

The first application of this ENA technique by Roelof et al.[66] took hourly averages of all the ENA flux viewed from ISEE-1 at 20 R_e during the recovery phase of a small geomagnetic storm (17 December 1977). The decay rate of the ENA flux was slower than that expected from hydrogen, so they concluded that the MEPI was responding mainly to oxygen atoms. Since the Dessler–Parker relation (Eq. 6) implies that the observed dD_{st}/dt is proportional to the measured ENA flux, they could demonstrate that the dominant mechanism for the recovery of the storm was charge-exchange loss of O^+ ions from the ring current. Much better detailed imaging was possible during the main phase of a large geomagnetic storm on 29 September 1978; ISEE-1 was at a high magnetic latitude (51.5°) near the dawn meridian (0730 MLT) at a radius of 2.6 R_e. The spacecraft location relative to the ring-current population is shown in Fig. 15; the shaded area corresponds to $3 < L < 5$. ISEE-1 was outside the ring current ($L = 6.7\ R_e$) and hence the MEPI responded almost exclusively to ENA. When the 5-min ENA image was obtained (0955 to 1000 UT), the average depression in the surface magnetic field strength measured by equatorial observatories was −241 nT.

The analysis of this ENA image by Roelof[67] is summarized in Fig. 16. All panels are "fish-eye" projections

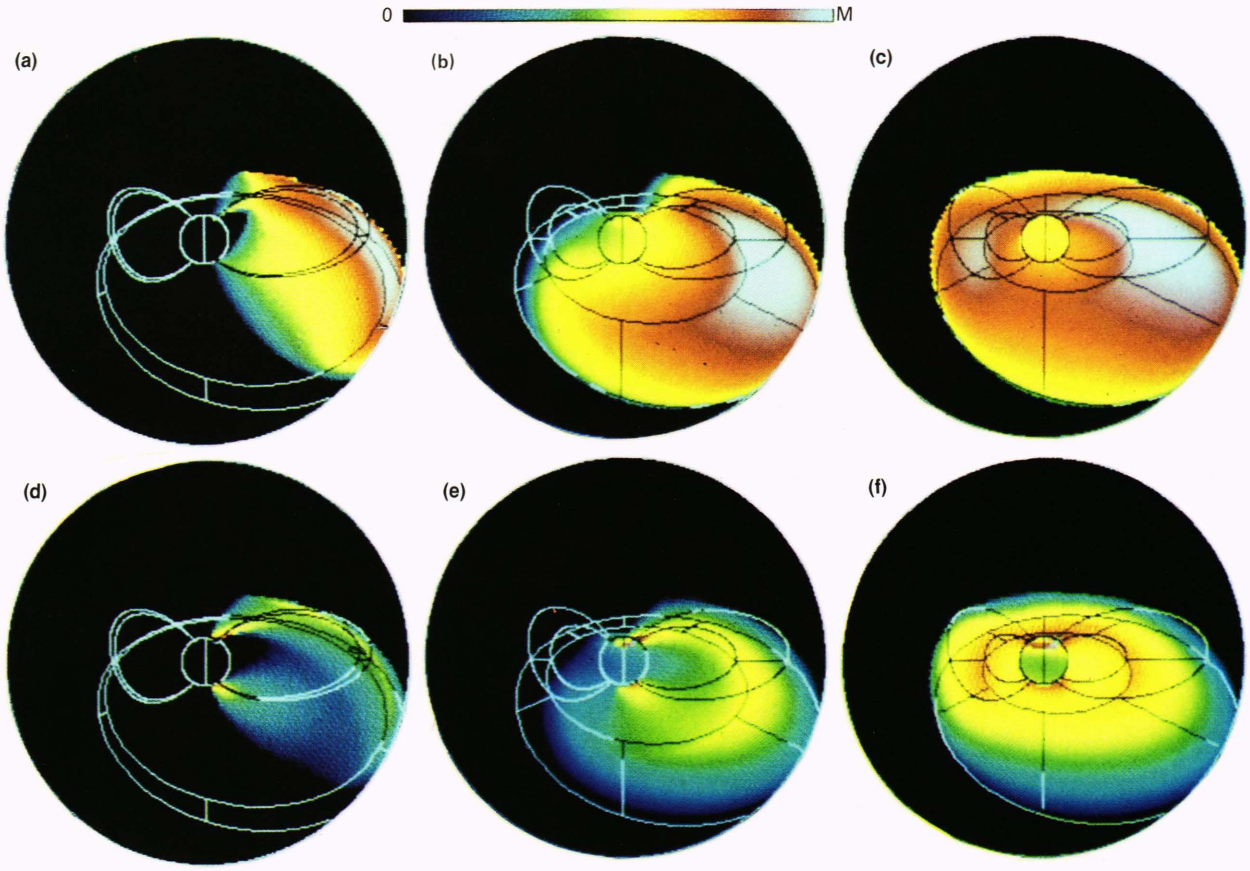

Figure 14 — (a to c) False-color images of model ring-current ion intensity evolution. Color represents the column-integrated flux of ions whose instantaneous velocity vector points toward the viewing point. Panels correspond to injection times t_1 to t_3, modeled in Fig. 13. Closed contours indicate the equatorial crossing locus of the inner and outer L shells containing the model fluxes. Magnetic local time cuts at every 3 hours (45°) connect the equatorial loci, with 1800 MLT being the lower vertical line; the sun is to the left. The linear color bar runs from zero to the maximum (M). The viewing point is at a radius of 8 R_e and 30° geomagnetic latitude in the dusk meridian plane. (d to f) False-color images of the ENA flux arising from the modeled interaction of the ions in a to c with the hydrogen geocorona. Same format as a to d.

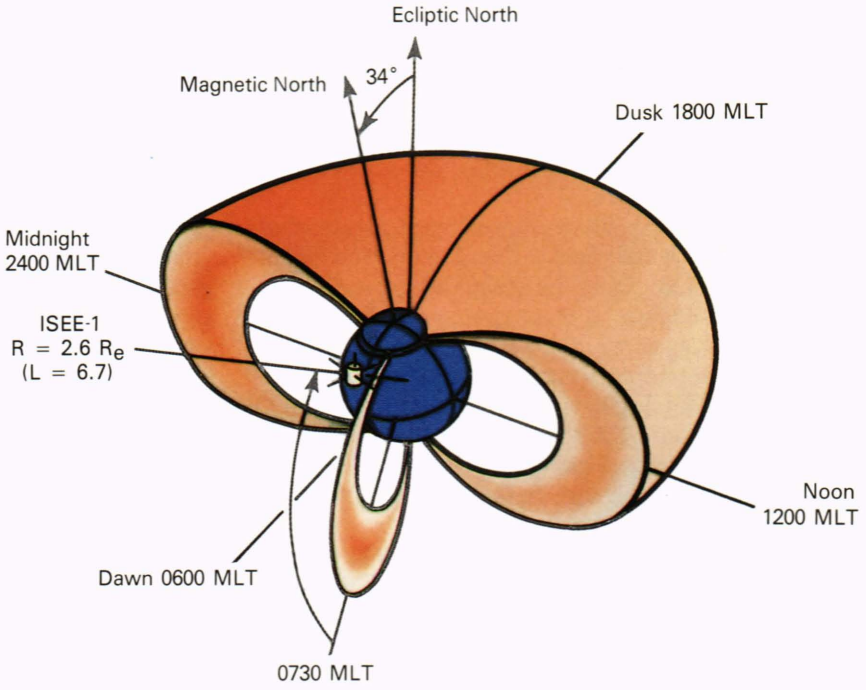

Figure 15 — Position of the ISEE-1 spacecraft relative to the ring-current ion population ($3 < L < 5$) at 1000 UT, 29 September 1978, during a large geomagnetic storm. ISEE-1 was outside the ring-current region and hence could measure ENA.

of the earthward hemisphere of the sky. The earth disk and its terminator are outlined; circles in the magnetic equator at 3 and 5 R_e are connected by radial lines every 3 hours of magnetic local time, including noon (which is to the right). Magnetic field lines for $L = 3$ and 5 are drawn in the planes of magnetic noon, dusk, midnight (to the left), and dawn (toward the reader). A common linear color bar is used, and its maximum value is indicated in each panel.

The ENA data are given in Fig. 16d. As described above, the MEPI on ISEE-1 scans the entire sky in 12 spins of the spacecraft. Data are grouped into 16 angular sectors of 22.5° during each spin, so the ENA flux is binned into 192 "pixels," each 22.5° by 13.3°. The color code in Fig. 16d gives the average number of ENA counts each time a pixel is read out; for example, in the middle (green–yellow) range, there are 15 counts per accumulation. The accumulation time is 3/16 s, which corresponds to a rate of 80 ENA/s. The MEPI energy channel used corresponds to 24 to 34 keV for H and 60 to 77 keV for O.

The ENA image reveals the very dramatic midnight–noon asymmetry, and thus this single image immediately established that the storm-time ring current was certainly not axisymmetric, as had often been assumed in early studies.

To extract the actual ion fluxes from the ENA image requires a computer simulation using a model ring-current ion distribution function. A single ENA image cannot be inverted directly, because the three-dimensional ion distribution has been collapsed along the line of sight and weighted by the hydrogen geocoronal density (see Eq. 14). Consequently, the following procedure was used to extract the ion distribution:

1. A model ion distribution function was chosen, specified by the smallest possible number of adjustable parameters that still allow a physically reasonable function. The column-integrated ion flux (as in Fig. 11) is shown in Fig. 16a for the parameters eventually selected. Note the strong excess of ion flux in the midnight sector.
2. The model j_{ion} fluxes were used in Eq. 14 to calculate model j_{ena} fluxes using the geocoronal H-atom density curve of Rairden et al.[57] (Fig. 11). These ENA fluxes are shown in Fig. 16b and can be scaled by the one parameter remaining free, the maximum ion flux j_{max} in the ring current.
3. The model ENA flux was then passed through the MEPI "telescope" function, which degraded the angular resolution to pixels 22.5° by 13.3°. The counts in these pixels yielded the simulated image shown in Fig. 16c. The model parameters for j_{ion} were adjusted until the simulated ENA image in Fig. 16c appeared similar to the observed ISEE-1 ENA image (Fig. 16d).
4. Once the relative count contours agreed, the absolute brightness was adjusted using the one remaining parameter, j_{max}, so that the number of counts in each pixel of the simulation agreed with those in the corresponding pixel of the observed image to the maximum extent possible.

The model ring-current distribution finally obtained for the ISEE-1 image of 0955 to 1000 UT, 29 September 1978, has the ions confined to field lines of $3 < L < 5$, and an exponential cosine-dependence on longitude with a 33:1 midnight-to-noon ratio. An isotropic pressure tensor gave the best fit. Assuming the MEPI fluxes were dominated by O atoms, as is suggested by the shape of the ENA spectrum, the maximum ion flux in the ring current (at $L = 4$ at magnetic midnight) was $1 \times 10^{10}/m^2 \cdot s \cdot sr \cdot keV$ at 70 keV. Although there have been

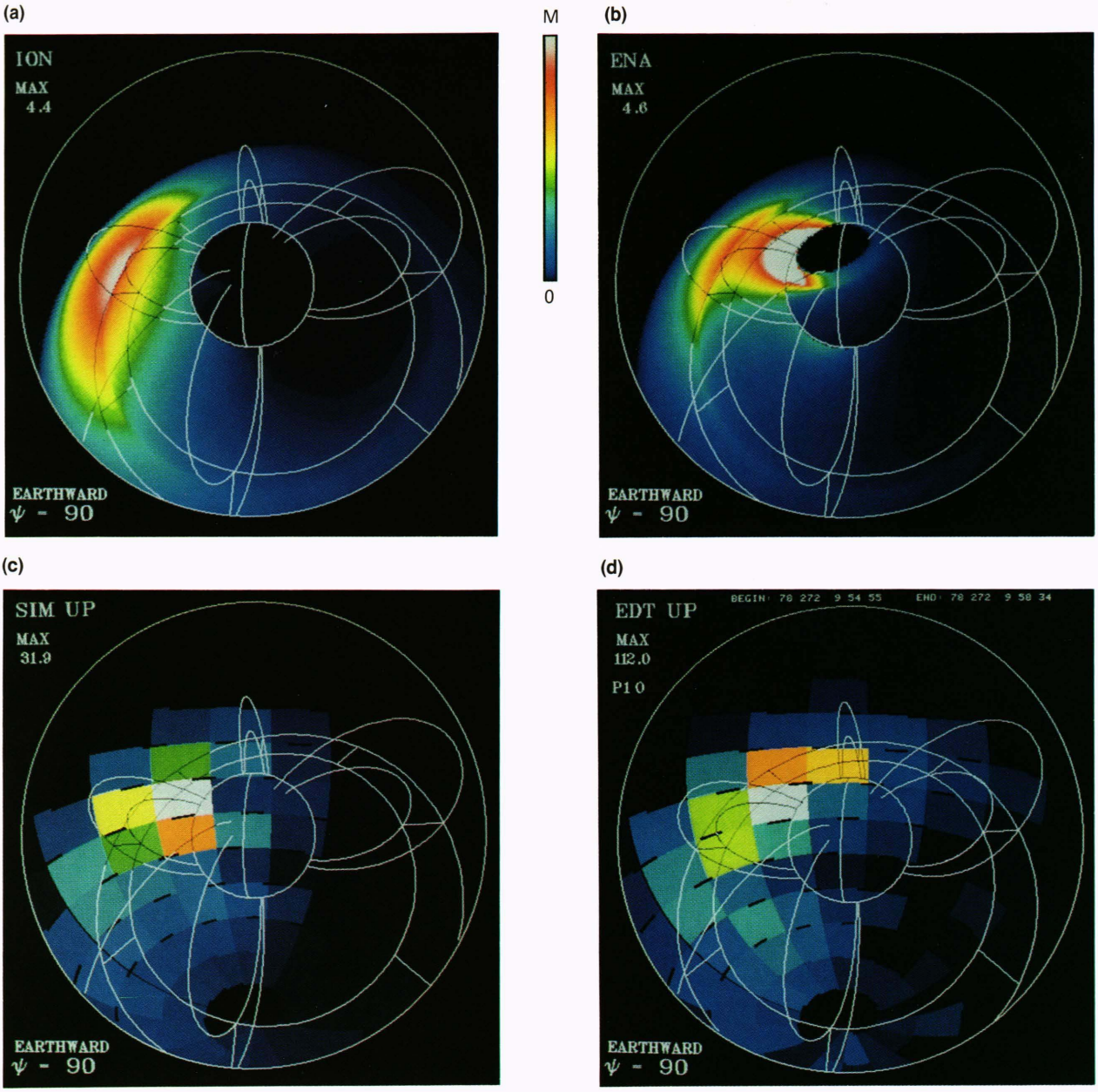

Figure 16 — Models, simulation, and measurement[67] of an ENA image of the storm-time ring-current ion population, represented in the earthward hemisphere viewed from the ISEE-1 spacecraft: (a) Column-integrated ion differential flux from the model ring current. (b) ENA flux computed from the model ring-current ion distribution in Fig. 16a; color-bar saturated at low altitudes. (c) Simulated MEPI rates (average counts per pixel) computed from model ENA fluxes of Fig. 16b. (d) Actual MEPI image from 0955 to 1000 UT, 29 September 1978. MAX values are color-bar maxima.

no *in situ* composition measurements in the midnight sector during large storms, this flux appears reasonable when compared with the smaller *in situ* measurements obtained at other locations in other (and usually smaller) storms.

A further check of consistency can be obtained from the Dessler–Parker relation given by Eq. 6. The total energy in the model ring-current oxygen ions, with $j_{max} = 1 \times 10^{10}/m^2 \cdot s \cdot sr \cdot keV$, is approximately 6.6×10^{15} J. As noted earlier, it requires about 4×10^{13} J in the ring current to produce a 1-nT depression in the equatorial surface field. Thus, the oxygen component of the ring current should have caused about a 160-nT effect. The total observed was $D_{st} = -241$ nT. This would leave about 80 nT to be produced by the proton component. In smaller storms observed on the day side, the energy density of protons exceeded that of the oxygen.[32] As mentioned in the section on composition, however, the O^+/H^+ ratio appears to increase with geomagnetic activity. Overall, the deductions of global morphology and intensity of the ring-current ions obtained from the global ENA images seem to be consistent with the *in situ* measurements, once the spatial dependence and storm size are taken into account.

THE FUTURE OF ENA OBSERVATIONS

The ENA images were obtained from the MEPI ion telescope on ISEE-1, an instrument that certainly was not optimized for ENA observations. What might be done with an instrument specifically designed for ENA imaging? We gave our impression of the global information such an instrument could provide in the section on ENA imaging. Recently, we have presented concepts for the future generation of ENA images at a topical conference, and we refer the interested reader to the resulting publications.[68-71] Let us conclude with a computer simulation of what an idealized ENA imager with $1° \times 1°$ angular resolution might have obtained if it had viewed the storm of 29 September 1978 from different locations in the magnetosphere.

We have chosen positions along a geographic polar orbit every 15° of (geographic) latitude from 60°N to 75°S; the latter happens to be approximately over the south magnetic pole. The orbit drawn in Fig. 17 has an apogee of $r = 9\ R_e$ and a perigee of 1000 km. The images are computed from the model ring-current ion distribution derived from the MEPI ENA observations of 29 September 1978 and are shown in Figs. 18a through 18i in the same format as Fig. 16b. To bring out the global morphology more definitively, however, a logarithmic color bar is used, spanning a factor of 100 in intensity and normalized to the brightest part of the image. The maximum brightness is indicated by the number labeled "MAX." No attempt is made to model accurately the complex interaction of ions and ENA with the exosphere below an altitude of 1000 km.

We offer the following brief comments on each ENA image:

Figure 18a: 45°N, $r = 4.5\ R_e$. The strong midnight–noon asymmetry is clearly evident. The southern low-altitude emission comes into view, and the three-dimensional structure of the ring-current L-shells can be perceived.

Figure 18b: 30°N, $r = 3.3\ R_e$. This is almost the same view as from ISEE-1 (see Fig. 16b), but in the dusk meridian.

Figure 18c: 15°N, $r = 2.5\ R_e$. The midnight L-shells are seen nearly edge-on.

Figure 18d: Geomagnetic equator, $r = 2.0\ R_e$.

Figure 18e: 15°S, $r = 1.7\ R_e$. The northern low-altitude emission region is nearly eclipsed.

Figure 18f: 30°S, $r = 1.5\ R_e$. The southern subauroral zone is in view.

Figure 18g: 45°S, $h = 2000$ km. The spacecraft is actually within the ring current, but the local production is too weak to register. The distant "limb" of the $L = 3$ shell is clearly delineated, however.

Figure 18h: 60°S, $h = 1400$ km. The ring current is now viewed from below the $L = 5$ shell. A complex limb effect exists in the midnight sector.

Figure 18i: 75°S, $h = 1100$ km. Viewed from near the south pole. The midnight–noon asymmetry is quite apparent, even at low altitude.

A review of Figs. 18a to 18i shows that much valuable and quantitative global information on the structure of the ring current can be obtained at a variety of orbital positions, such as polar latitudes at $r = 6\ R_e$, equatorial latitudes at 2 to 3 R_e, and polar latitudes at 1000-km altitude. ENA imaging as a tool for understanding the morphology and dynamics of the global ring-current ion population is clearly just beginning to reveal its full potential.

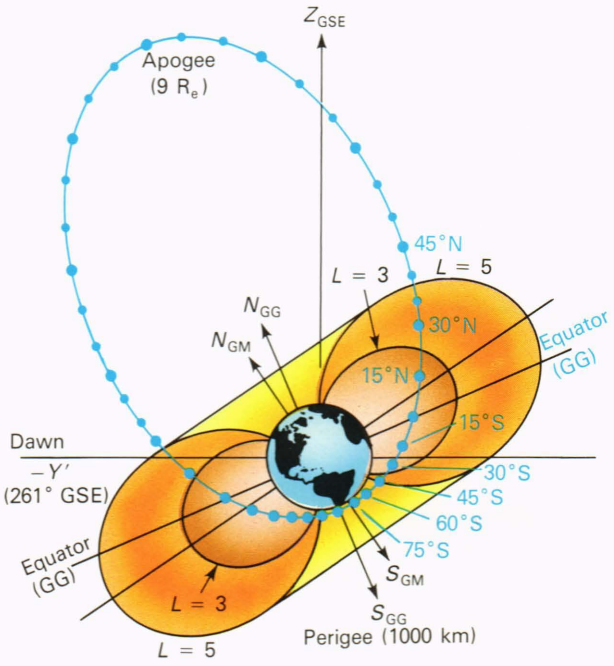

Figure 17 — A hypothetical polar orbit for simulated viewing of ENA fluxes. Positions labeled with geographic latitude correspond to images in Fig. 18.

REFERENCES

1. T. A. Potemra, "Magnetospheric Currents," *Johns Hopkins APL Tech. Dig.* **4**, 276–284 (1983).
2. C. F. Kennell, L. J. Lanzerotti, and E. N. Parker, eds., *Solar System Plasma Physics*, Vol. III, North-Holland Pub. Co., 317–371 (1979).
3. R. W. McEntire, "An Update on the Active Magnetospheric Particle Tracer Explorers (AMPTE) Program," *Johns Hopkins APL Tech. Dig.* **8**, 340–347 (1987).
4. See the seven AMPTE/CCE papers in the special issue of *Geophys. Res. Lett.* **12** (1985).
5. See the historical material in C. Störmer, *The Polar Aurora*, Oxford Univ. Press, London and New York (1955).
6. A. Schmidt, "Das Erdmagnetische Aussenfeld," *Zeitschrift für Geophysik*, **1**, 1–13 (1924).
7. S. Chapman and V. C. A. Ferraro, "A New Theory of Magnetic Storms," *Terr. Magn. Atmos. Elec.*, **36**, 77–97 and 171–186 (1931); **37**, 147–156 and 421–429 (1932); **38**, 79–96 (1933).
8. H. Alfvén, "On the Electric Field Theory of Magnetic Storms and Aurorae," *Tellus* **7**, 54 (1955).
9. E. N. Parker, "Newtonian Development of the Dynamical Properties of Ionized Gases at Low Density," *Phys. Rev.* **107**, 924 (1957).
10. S. F. Singer, "A New Model of Magnetic Storms and Aurorae," *Trans. Am. Geophys. Union* **38**, 175 (1957).
11. A. J. Dessler and E. N. Parker, "Hydromagnetic Theory of Geomagnetic Storms," *J. Geophys. Res.* **64**, 2239 (1959).
12. S.-I. Akasofu and S. Chapman, "The Ring Current, Geomagnetic Disturbance, and the Van Allen Radiation Belts," *J. Geophys. Res.* **66**, 1321 (1961).
13. J. R. Apel, S. F. Singer, and R. C. Wentworth, "Effects of Trapped Particles on the Geomagnetic Field," *Adv. Geophysics* **9**, 131 (1962).
14. R. A. Hoffman and P. A. Bracken, "Higher-Order Ring Currents and Particle Energy Storage in the Magnetosphere," *J. Geophys. Res.* **72**, 6039 (1967).
15. L. A. Frank, "Several Observations of Low Energy Protons and Electrons in the Earth's Magnetosphere with OGO 3," *J. Geophys. Res.* **72**, 1905 (1967).

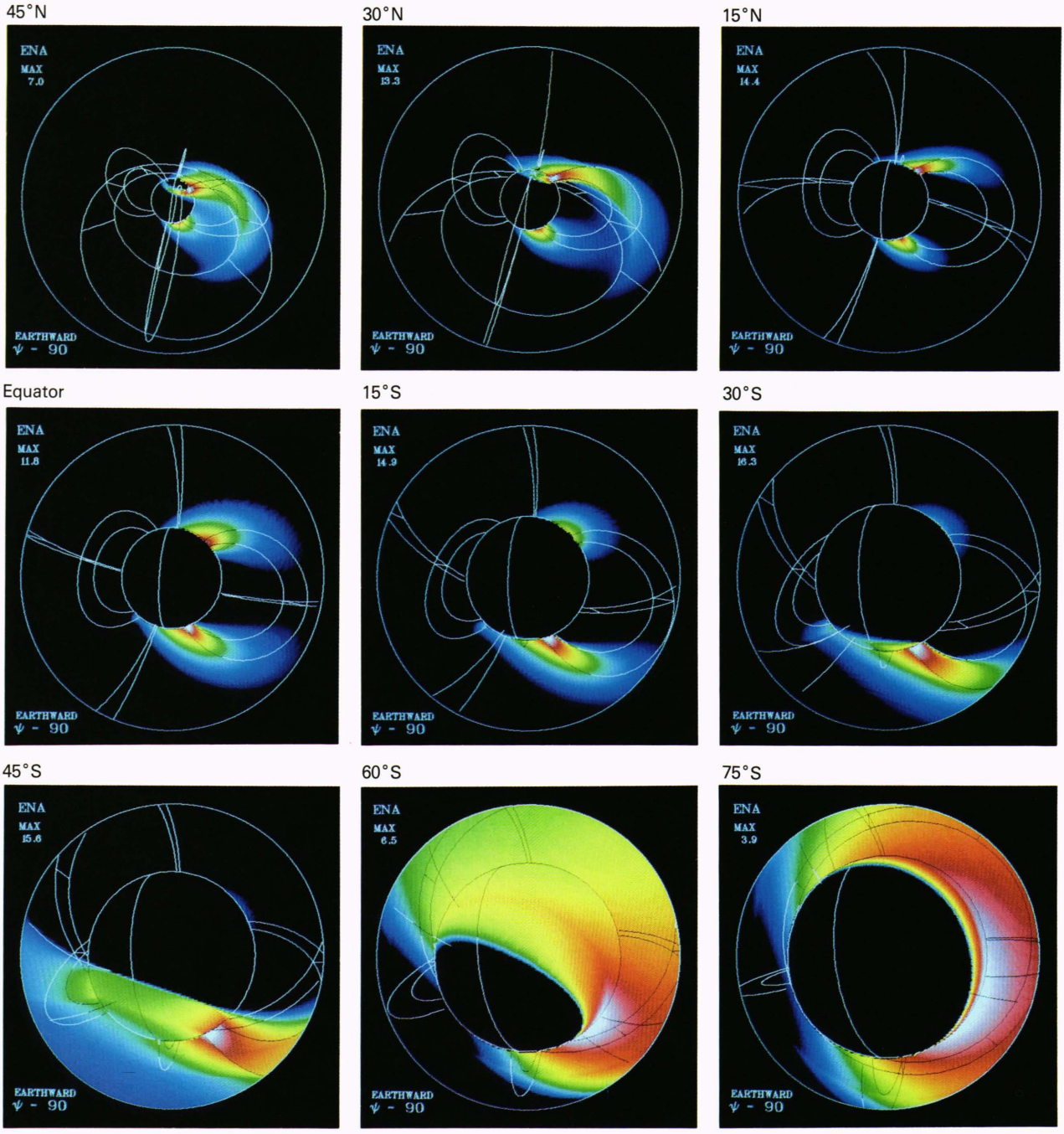

Figure 18 — Computer-simulated ENA images with 1° × 1° angular resolution. Views are earthward hemisphere from spacecraft positions drawn in Fig. 17. The logarithmic color-bar spans from the most intense ENA flux to 1% of that flux; the MAX value (absolute dimensionless units) for each panel indicates maximum brightness. Contours against the sky are as follows: circles in the magnetic equator at $r = 3\ R_e$ and $r = 5\ R_e$; equatorial lines of constant magnetic longitude every 45° (beginning with noon, to left); and magnetic field lines $L = 3$ and 5 in magnetic dawn, noon, dusk, and midnight meridians. The earth terminator is indicated, sun to the left. Model ENA fluxes, showing strong midnight-noon asymmetry (33:1), were computed from a ring-current model deduced from actual ENA measurement[67] during the geomagnetic storm from 0955 to 1000 UT, 29 September 1978 (see Fig. 16).

[16]L. A. Frank, "On the Extraterrestrial Ring Current During Geomagnetic Storms," *J. Geophys. Res.* **72**, 3753 (1967).
[17]P. H. Smith and R. A. Hoffman, "Ring Current Particle Distribution during the Magnetic Storms of December 16–18, 1971," *J. Geophys. Res.* **78**, 4731 (1973).
[18]L. R. Lyons and D. J. Williams, "Storm Associated Variations of Equatorially Mirroring Ring Current Protons, 1–800 keV, at Constant First Adiabatic Invariant," *J. Geophys. Res.* **81**, 216 (1976).
[19]D. J. Williams, "Ring Current Composition and Sources," in *Dynamics of the Magnetosphere,* S.-I. Akasofu, ed., D. Reidel Pub. Co., Dordrecht, Holland, 407 (1980).
[20]N. Sckopke, "A General Relation between the Energy of Trapped Particles and the Disturbance Field near the Earth," *J. Geophys. Res.* **71**, 3125 (1966).
[21]R. L. Carovillano and J. J. Maguire, "Magnetic Energy Relationships in the

Magnetosphere," in *Physics of the Magnetosphere,* R. L. Carovillano, J. F. McClay, and H. R. Radoski, eds., D. Reidel Pub. Co., Dordrecht, Holland, 290 (1968).
[22]S. Olbert, G. L. Siscoe, and V. M. Vasyliunas, "A Simple Derivation of the Dessler-Parker-Sckopke Relation," *J. Geophys. Res.* **73**, 1115 (1968).
[23]R. L. Carovillano and G. L. Siscoe, "Energy and Momentum Theorems in Magnetospheric Processes," *Rev. Geophys. Space Phys.* **11**, 289 (1973).
[24]V. M. Vasyliunas, "Mathematical Models of Magnetosphere Convection and Its Coupling to the Ionosphere," in *Particles and Fields in the Magnetosphere,* B. M. McCormac, ed., Springer-Verlag, New York, 60–71 (1970).
[25]E. C. Roelof (abstract), "Global Topology of Electrical Currents Deduced from ENA Images of Storm-Time Ring Current Ions," *Eos* **69** (in press).
[26]L. J. Zanetti, B. H. Mauk, A. T. Y. Lui, T. A. Potemra, E. C. Roelof, and T. Iijima, "The Equatorial Ring Current as Determined from AMPTE/CCE and ISEE-1: Implications on Modelling Efforts," *Eos* **69** (in press).
[27]D. J. Williams, "Phase Space Variations of Equatorially Mirroring Ring Current Ions," *J. Geophys. Res.* **86**, 189 (1981).
[28]D. J. Williams, "Ring Current Composition and Sources: An Update," *Planet. Space Sci.* **29**, 1195 (1981).
[29]A. T. Y. Lui, R. W. McEntire, and S. M. Krimigis, "Evolution of the Ring Current During Two Geomagnetic Storms," *J. Geophys. Res.* **92**, 7459–7470 (1987).
[30]D. T. Young, H. Balsiger, and J. Geiss, "Correlations of Magnetospheric Ion Composition with Geomagnetic and Solar Activity," *J. Geophys. Res.* **87**, 9077–9096 (1982).
[31]G. Gloeckler, B. Wilken, W. Studemann, F. M. Ipavich, D. Hovestadt, D. C. Hamilton, and G. Kremser, "First Composition Measurements of the Bulk of the Storm Time Ring Current (1 to 300 keV/e) with AMPTE-CCE," *Geophys. Res. Lett.* **12**, 325–328 (1985).
[32]S. M. Krimigis, G. Gloeckler, R. W. McEntire, T. A. Potemra, F. L. Scarf, and E. G. Shelley, "Magnetic Storm of 4 September 1985: A Synthesis of Ring Current Spectra and Energy Densities Measured with AMPTE-CCE," *Geophys. Res. Lett.,* **12**, 329–332 (1985).
[33]W. Stüdemann, G. Gloeckler, B. Wilken, F. M. Ipavich, G. Kremser, and D. C. Hamilton, "Ion Composition of the Bulk Ring Current During a Magnetic Storm: Observations with the CHEM-Instrument on CHEM/CCE," in *Solar Wind-Magnetosphere Coupling,* Y. Kamide and J. A. Slavin, eds., Terra Scientific (Tokyo), 697–706 (1985).
[34]R. W. McEntire, A. T. Y. Lui, S. M. Krimigis, and E. P. Keath, "AMPTE/CCE Particle Composition Measurements during the September 4, 1984 Magnetic Storm," *Geophys. Res. Lett.* **12**, 317–320 (1985).
[35]G. Kremser, W. Stüdemann, B. Wilken, G. Gloeckler, D. C. Hamilton, F. M. Ipavich, and D. Hovestadt, "Charge State Distributions of Oxygen and Carbon in the Energy Range 1 to 300 keV/e Observed with AMPTE/CCE in the Magnetosphere," *Geophys. Res. Lett.* **12**, 847–850 (1985).
[36]G. Kremser, W. Stüdemann, B. Wilken, G. Gloeckler, D. C. Hamilton, and F. Ipavich, "Average Spatial Distributions of Energetic O^+, O^{2+} O^{6+}, and C^{6+} Ions in the Magnetosphere Observed by AMPTE CCE," *J. Geophys. Res.* **92**, 4459–4466 (1987).
[37]W. N. Spjeldvik, "Transport, Charge Exchange and Loss of Energetic Heavy Ions in the Earth's Radiation Belts: Applicability and Limitations of Theory," *Planet. Space Sci.* **29**, 1215–1226 (1981).
[38]P. D. Craven, R. C. Olsen, C. R. Chappel, and L. Kakani, "Observations of Molecular Ions in the Earth's Magnetosphere," *J. Geophys. Res.* **90**, 7599 (1985).
[39]B. Kleckler, E. Mobius, D. Hovestadt, M. Scholer, G. Gloeckler, and F. M. Ipavich, "Discovery of Energetic Molecular Ions (NO^+ and O_2^+) in the Storm Time Ring Current," *Geophys. Res. Lett.* **13**, 632 (1986).
[40]W. I. Axford, "Magnetospheric Convection," *Rev. Geophys.* **7**, 421 (1969).
[41]E. G. Shelley, R. D. Sharp, and R. G. Johnson, "Satellite Observations of an Ionospheric Acceleration Mechanism," *Geophys. Res. Lett.* **3**, 654 (1976).
[42]C. E. McIlwain, "Substorm Injection Boundaries," in *Magnetospheric Physics,* B. M. McCormac, ed., D. Reidel Pub. Co., Dordrecht, Holland, 143 (1974).
[43]B. H. Mauk and C. E. McIlwain, "Correlation of Kp with the Substorm-Injected Plasma Boundary," *J. Geophys. Res.* **79**, 3193 (1974).
[44]A. Konradi, C. L. Semar, and T. A. Fritz, "Substorm-Injected Protons and Electrons and the Injection Boundary Model," *J. Geophys. Res.* **80**, 543 (1975).
[45]M. E. Greenspan, D. J. Williams, B. H. Mauk, and C.-I. Meng, "Ion and Electron Energy Dispersion Features Detected by ISEE-1," *J. Geophys. Res.* **90**, 4079–4089 (1985).
[46]M. G. Kivelson, "Magnetospheric Electric Fields and Their Variation with Geomagnetic Activity," *Rev. Geophys. Space Phys.* **14**, 189 (1976).
[47]M. G. Kivelson, S. M. Kaye, and D. J. Southwood, "Approximations for the Study of Drift Boundaries in the Magnetosphere," *J. Geophys. Res.* **80**, 3528 (1975).
[48]M. G. Kivelson, S. M. Kaye, and D. J. Southwood, "The Physics of Plasma Injection Events," in *Dynamics of the Magnetosphere,* S.-I. Akasofu, ed., D. Reidel Pub. Co., Dordrecht, Holland, 385 (1980).
[49]B. H. Mauk and C.-I. Meng, "Characterization of Geostationary Particle Signatures Based on the 'Injection Boundary' Model," *J. Geophys. Res.* **88**, 3055–3071 (1983).
[50]B. H. Mauk and C.-I. Meng, "Dynamical Injections as the Source of Near Geostationary, Quiet-Time Particle Spatial Boundaries," *J. Geophys. Res.* **88**, 10011–10024 (1983).
[51]L. R. Lyons and D. J. Williams, "A Source for the Geomagnetic Storm Main Phase Ring Current," *J. Geophys. Res.* **85**, 523 (1980).
[52]A. T. Y. Lui, R. W. McEntire, S. M. Krimigis, and E. P. Keath, "Acceleration of Energetic Oxygen ($E > 137$ keV) in the Storm-Time Ring Current," in *Ion Acceleration in the Magnetosphere and Ionosphere, Geophys. Monogr. Ser.,* Vol. 38, T. Chang, ed., American Geophysical Union, Washington (1986).
[53]B. H. Mauk and C.-I. Meng, "Macroscopic Ion Acceleration Associated with the Formation of the Ring Current in the Earth's Magnetosphere," in *Ion Acceleration in the Magnetosphere and Ionosphere, Geophys. Monogr. Ser.,* Vol. 38, T. Chang, ed., American Geophysical Union, Washington (1986).
[54]G. W. Stuart, "Satellite Measured Radiation," *Phys. Rev. Lett.* **2**, 417 (1959).
[55]R. C. Wentworth, W. M. MacDonald, and S. F. Singer, "Lifetimes of Trapped Auroral Radiation Belt Particles," *Bull. Am. Phys. Series* 2, 4, 7 (1959).
[56]R. C. Wentworth, W. M. MacDonald, and S. F. Singer, "Lifetimes of Trapped Radiation Belt Particles Determined by Coulomb Scattering," *Phys. Fluids,* **2**, 499 (1959).
[57]R. L. Rairden, L. A. Frank, and J. D. Cruven, "Geocoronal Imaging with Dynamics Explorer," *J. Geophys. Res.* **91**, 13613–13630 (1986).
[58]P. H. Smith, N. K. Bewtra, and R. A. Hoffman, "Inference of the Ring Current Ion Composition by Means of Charge Exchange Decay," *J. Geophys. Res.* **86**, 3470 (1981).
[59]J. M. Cornwall, F. V. Coroniti, and R. M. Thorne, "Turbulent Loss of Ring Current Protons," *J. Geophys. Res.* **75**, 4699 (1970).
[60]D. J. Williams and L. R. Lyons, "The Proton Ring Current and Its Interaction with the Plasmapause: Storm Recovery Phase," *J. Geophys. Res.* **79**, 4195 (1974).
[61]D. J. Williams and L. R. Lyons, "Further Aspects of the Proton Ring Current Interaction with the Plasmapause: Main and Recovery Phases," *J. Geophys. Res.* **79**, 4791 (1974).
[62]D. J. Williams, G. Hernandez, and L. R. Lyons, "Simultaneous Observations of the Proton Ring Current and Stable Auroral Red Arcs," *J. Geophys. Res.* **81**, 608 (1976).
[63]J. M. Cornwall, F. V. Coroniti, and R. M. Thorne, "A Unified Theory for SAR Arc Formation at the Plasmapause," *J. Geophys. Res.* **76**, 4428 (1971).
[64]R. A. Phaneuf, compilation in preparation, Controlled Fusion Atomic Data Center, Oak Ridge National Laboratory, Oak Ridge, Tenn. (1988).
[65]D. J. Williams, E. Keppler, T. A. Fritz, and B. Wilken, "The ISEE 1 and 2 Medium Energy Particle Experiment," *IEEE Trans. Geosci. Electron.* **GE-16**, 270 (1978).
[66]E. C. Roelof, D. G. Mitchell, and D. J. Williams, "Energetic Neutral Atoms ($E \sim 50$ keV) from the Ring Current: IMP 7/8 and ISEE-1," *J. Geophys. Res.* **90**, 10991–11008 (1985).
[67]E. C. Roelof, "Energetic Neutral Atom Image of the Storm-Time Ring Current," *Geophys. Res. Lett.* **14**, 652–655 (1987).
[68]D. J. Williams, L. A. Frank, A. L. Broadfoot, W. L. Imhof, S. B. Mende, D. M. Hunten, R. G. Roble, and G. L. Siscoe, "Images of the Magnetosphere and Atmosphere: Global Effects (IMAGE)," proposal for NASA Explorer Mission Concept Studies (1986).
[69]E. P. Keath, G. B. Andrews, B. H. Mauk, D. G. Mitchell, and D. J. Williams, "Instrumentation for Energetic Neutral Atom Imaging of Magnetospheres," in *Proc. Yosemite 1988, Outstanding Problems in Solar System Plasma Physics; Theory and Instrumentation* (in press).
[70]R. W. McEntire and D. G. Mitchell, "Instrumentation for the Imaging of Energetic Neutral Atoms," in *Proc. Yosemite 1988, Outstanding Problems in Solar System Plasma Physics; Theory and Instrumentation* (in press).
[71]E. C. Roelof, "Energetic Neutral Atom Images of the Storm-Time Ring Current: ISEE-1 Observations and Computer Simulation," in *Proc. Yosemite 1988, Outstanding Problems in Solar System Plasma Physics; Theory and Instrumentation* (in press).

ACKNOWLEDGMENTS—The analysis of the ENA images from the MEPI on the ISEE-1 spacecraft has been supported by Grant NAGW-773 from the Earth Science and Applications Division, Space Plasma Physics Branch of NASA; from Grant ATM-8507084 from the Atmospheric Sciences Division, Solar Terrestrial Program of the National Science Foundation; and by NASA contract (D. J. Williams, Principal Investigator) to APL and the Department of the Navy under task I2UOS1C of Navy Contract N00039-87-C-5301.

THE AUTHORS

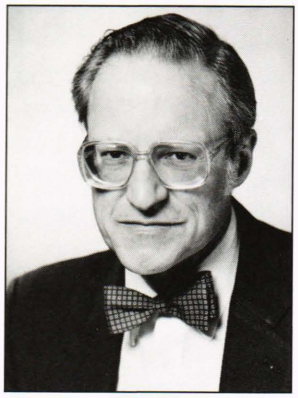

EDMOND C. ROELOF was born in Evanston, Ill., in 1937. He received his Ph.D. in physics from the University of California, Berkeley, in 1966. Dr. Roelof then was a research scientist at the Boeing Scientific Research Laboratories in Seattle and at NASA/Goddard Space Flight Center and an Assistant Professor of physics at the University of New Hampshire before joining APL's Space Physics and Instrumentation Group in 1974. He has held visiting appointments at NOAA's Space Environment Laboratory in Boulder, Colo., as well as at universities and institutes in The Netherlands, West Germany, and France. He has served on NASA Management Working Groups and as an officer of the American Geophysical Union, from which he received the 1987 Editor's Citation for Excellence in Refereeing (*Geophysical Research Letters*). His published research covers topics in energetic particles; plasma; magnetic fields; and radio emissions in the solar corona, the interplanetary medium, and the magnetospheres of Earth and Saturn. Dr. Roelof will continue these investigations through the 1990s as a co-investigator with the APL experimenter teams on the Ulysses (heliosphere), Galileo (Jupiter), and ISTP (Geotail) missions.

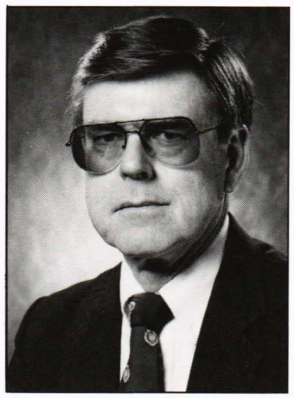

DONALD J. WILLIAMS was born in 1933. He received a B.S. degree in physics from Yale University in 1955 and, after two years in the Air Force, received M.S. and Ph.D. degrees in nuclear physics, also from Yale University, in 1958 and 1962, respectively. He joined APL's Space Department in 1961, where he participated in early space research activities. In 1965 he went to NASA/Goddard Space Flight Center, where he headed the Particle Physics Branch. In 1970 he was appointed Director of NOAA's Space Environment Laboratory in Boulder, Colo., where he remained until 1982 when he rejoined APL's Space Department.

Dr. Williams has been principal investigator, project scientist, and co-investigator for a variety of NASA, NOAA, DoD, and European satellite programs. His research activities are in the field of space plasma physics with emphasis on planetary magnetospheres. He has served on several national and international planning and advisory committees on space plasma physics and is Vice President of the International Association of Geophysics and Aeronomy. He is also principal investigator for the energetic particle detector on the NASA Galileo spacecraft, which will be launched to Jupiter in October 1989, and the energetic particle and ion composition experiment on the Japanese Geotail satellite, which will be launched into the earth's magnetotail regions in July 1992. Dr. Williams is Branch Chief of the Space Sciences Branch in the Space Department.